First high-accuracy, model-independent NRF measurements on ^{78,80}Kr to constrain photon strength functions for *p*-process nucleosynthesis calculations

&

Photoneutron cross section measurements on ^{94}Mo and ^{90}Zr relevant to the *p*-process nucleosynthesis

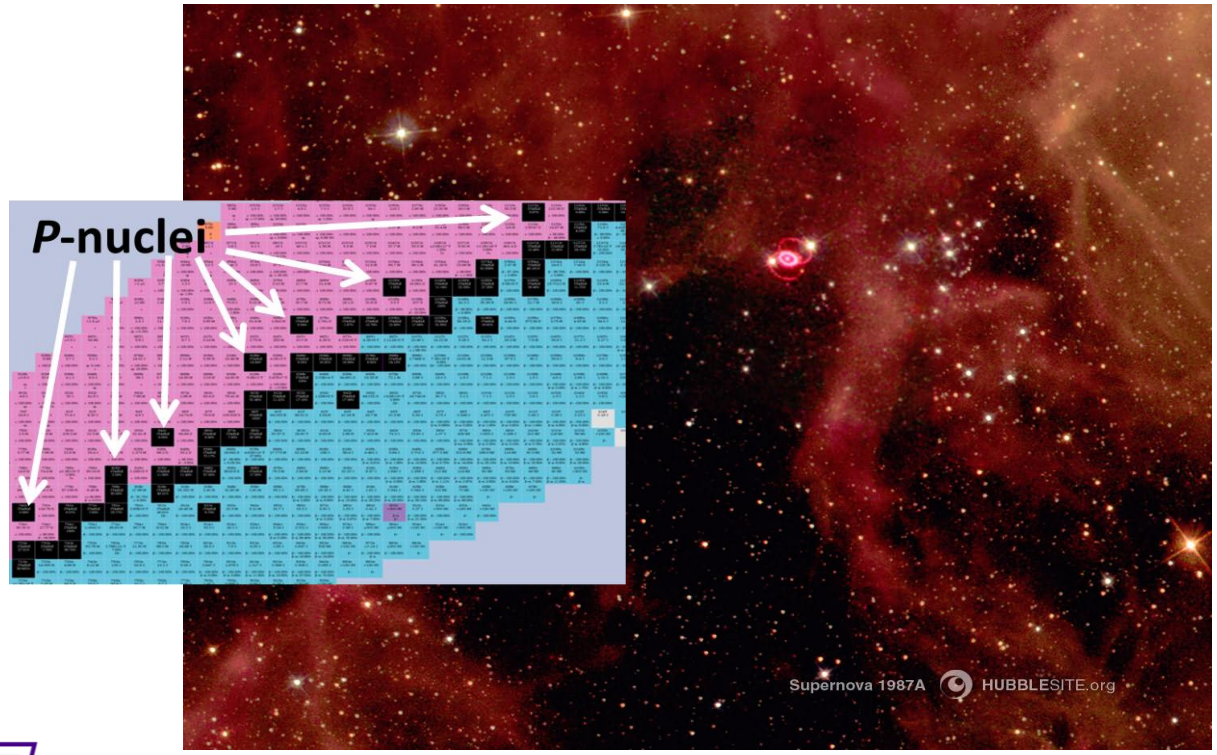

JMU
JAMES MADISON UNIVERSITY

The 5th Nuclear Photonics Conference
October 6-10, 2025, Darmstadt, Germany

JAMES MADISON UNIVERSITY PHYSICS AND ASTRONOMY

Collaborators:

A. M. Balbuena, R. L. Geissler, A. S. Kirk, E. G. Meekins,
B. E. A. Witczak (undergraduate students)
James Madison University, Department of Physics and Astronomy

S. W. Finch, F. Q. Friesen, U. Friman-Gayer(*), C. R. Howel,
R. V. F. Janssens, S. Johnson, H. J. Karwowski *et al.*
Triangle Universities Nuclear Laboratory (TUNL)
Duke University, University of North Carolina at Chapel Hill
(*) currently at Vysus Group Sweden AB, Malmö, Sweden

J.A. Silano
Nuclear and Chemical Sciences Division
Lawrence Livermore National Laboratory

S. Goriely
Institut d'Astronomie et d'Astrophysique (IAA)
Université Libre de Bruxelles

The various nucleosynthesis processes

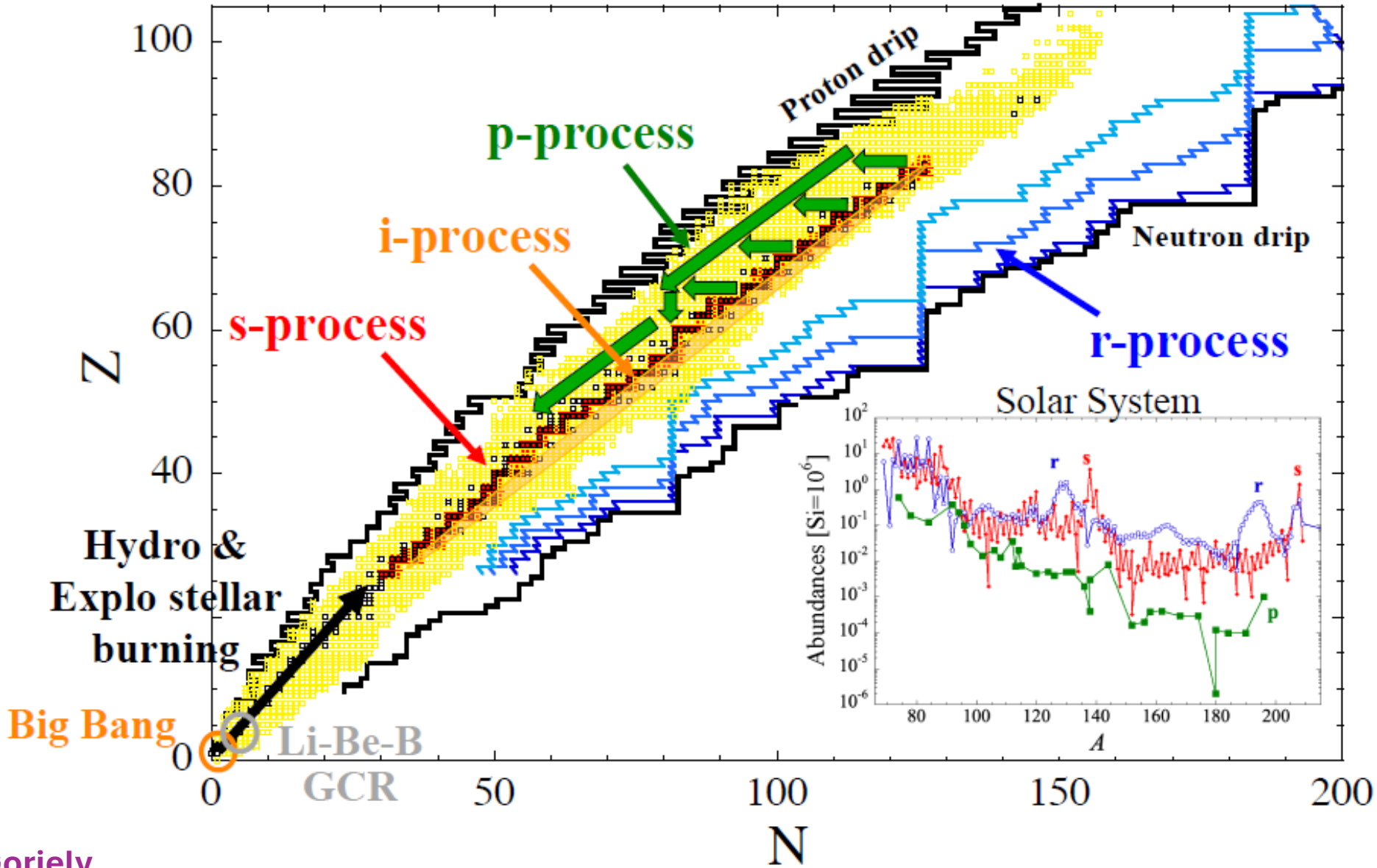

Credits: S. Goriely

The *p*-process is responsible for the nucleosynthesis beyond iron of ~35 proton-rich stable nuclei

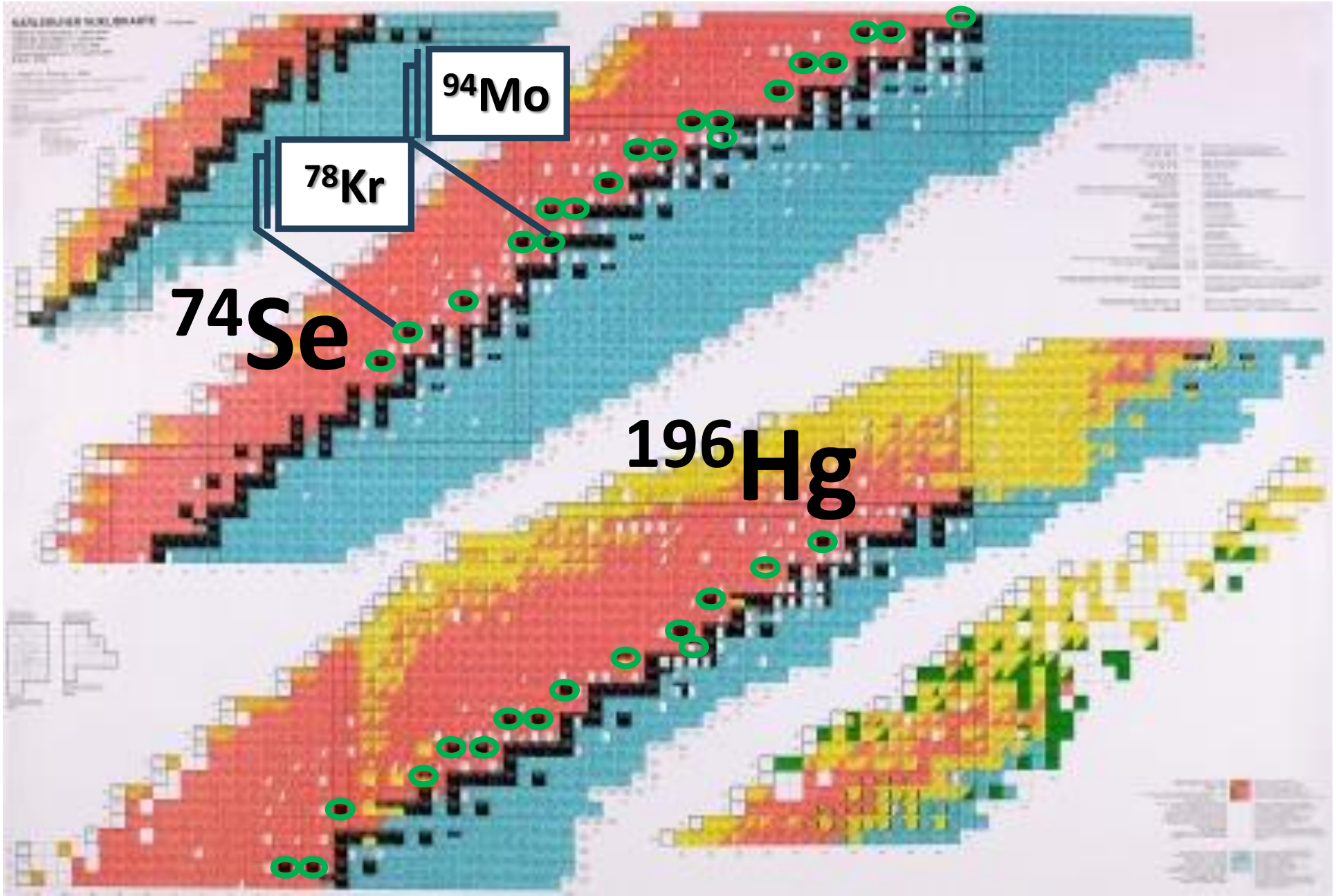

The *p*-Nuclei - 'nuclear astrophysics *p*-nuts'

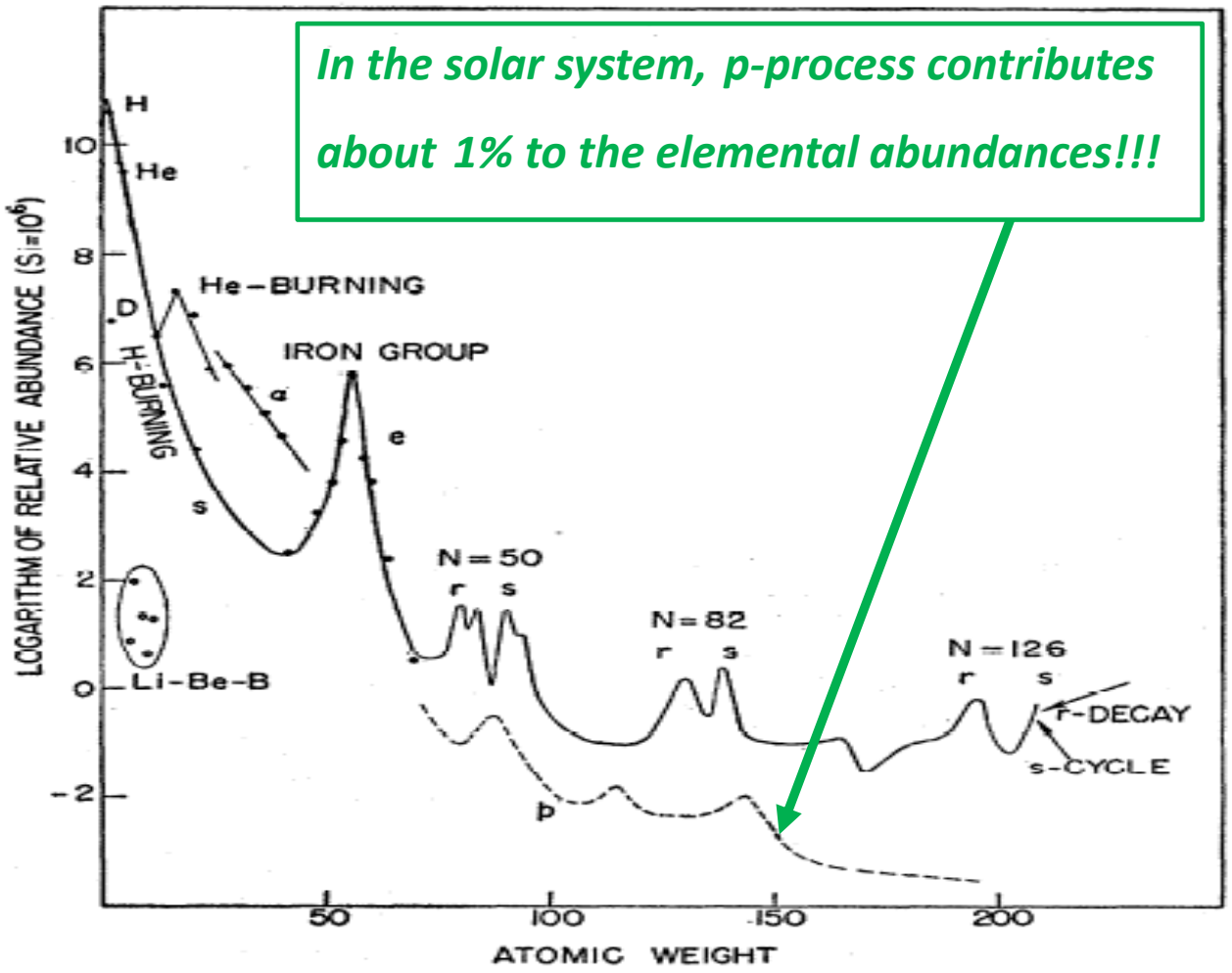

B²FH, Rev. Mod. Phys. 29, 547 (1957)

The *p*-process nucleosynthesis

- $\tau \sim 1s$ & $T \sim 2\text{-}3\ 10^9 K$
- Photodisintegrations (γ,n), (γ,p), (γ,α)
- SNII (O-Ne & νp-wind) & SNIa

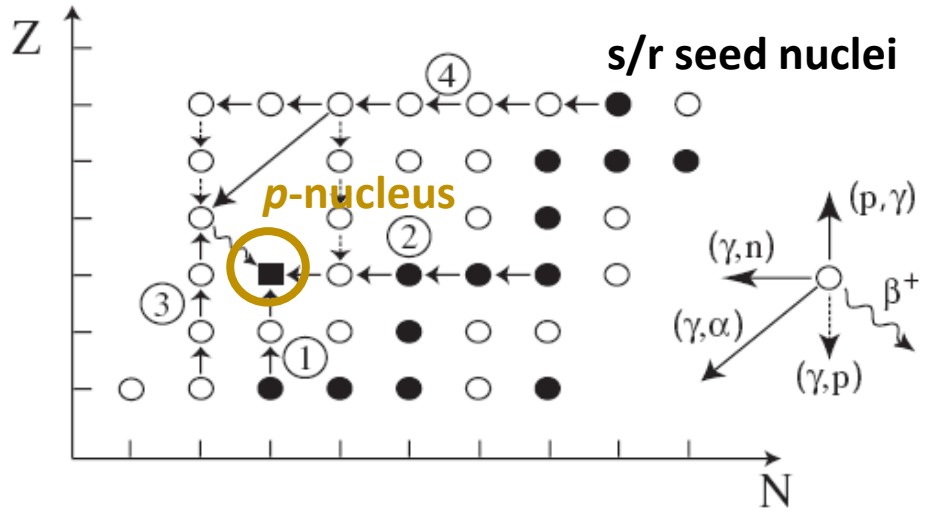

M. Arnould & S. Goriely, Phys. Rep. 384, 1 (2003)

***p*-Process Nucleosynthesis:**

an extended network of some 20000 reactions

linking about **2000 nuclei** in the A ≤ 210 mass range

- Photodisintegrations (γ,n), (γ,p), (γ,α)
- n-, p-, α-capture reactions
- β^+-decays

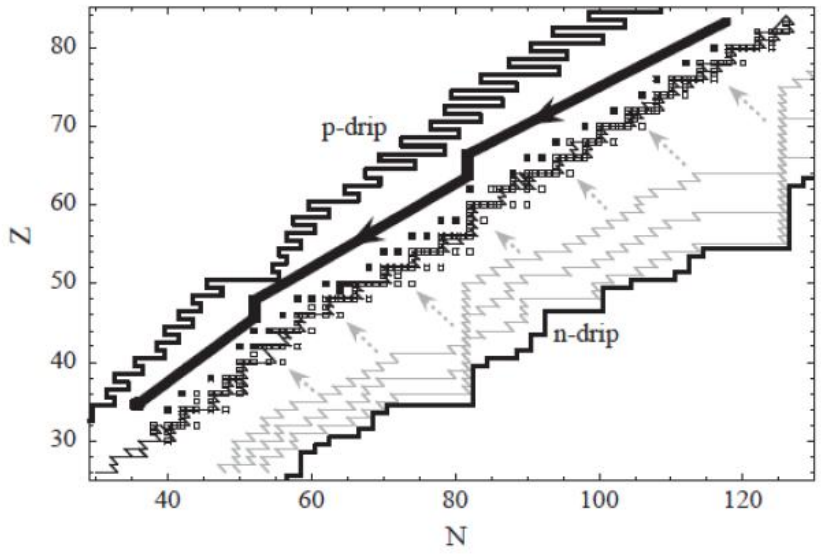

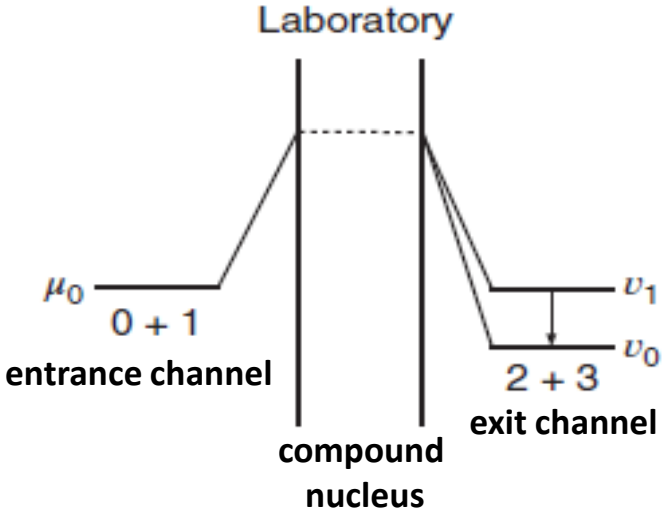

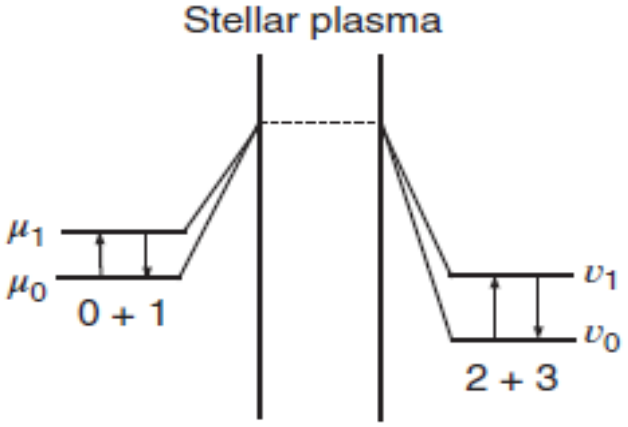

Image from C. Iliadis, Nuclear Physics of Stars (2007)

The **gs contribution** to the ***stellar rate*** for photodisintegration reactions concerning *p*-nuclei typically is only a few tenths per mille.

T. Rauscher, Ap. J. Suppl. 201, 26 (2012)

Photodisintegration experiments can only be used to derive information on certain nuclear properties required for the calculation of the stellar rates and, thus, to test and support the theory (statistical Hauser-Feshbach models)!!

- **Gamma-ray strength function**
- Nuclear level density
- Nucleon-nucleus optical potential

PHOTONUCLEAR REACTIONS

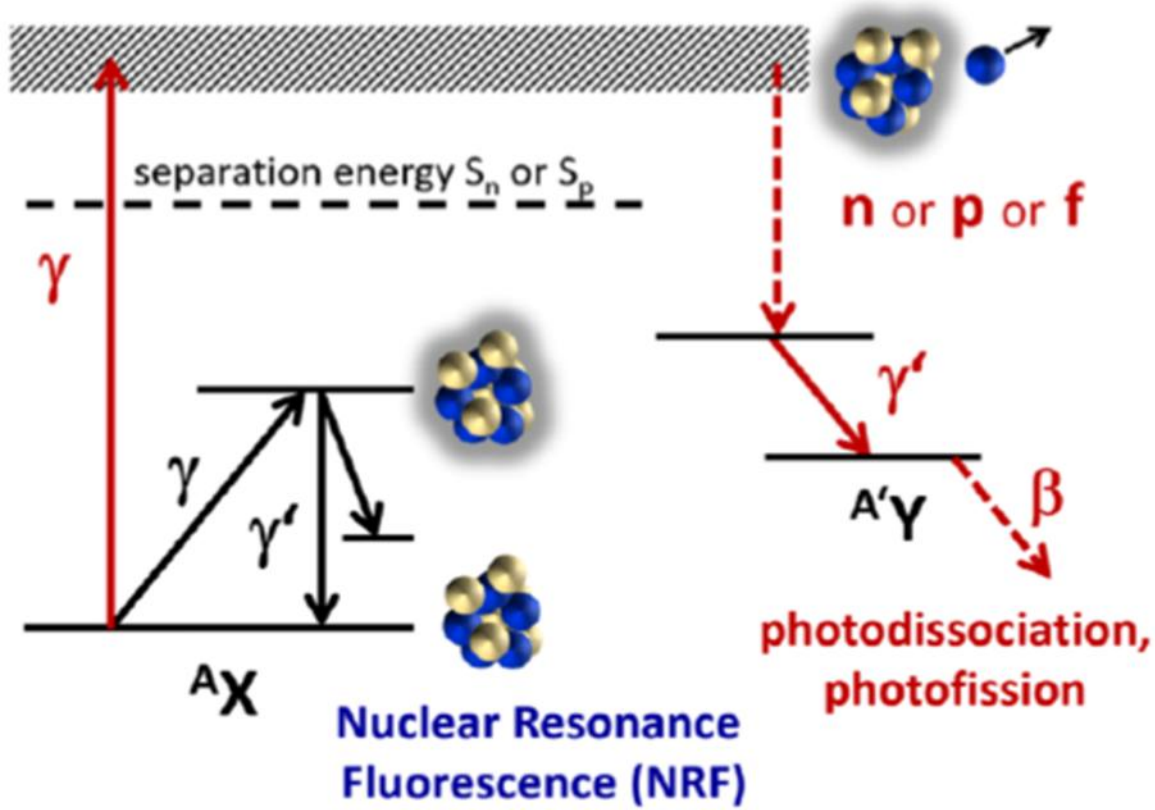

The reaction rate for a photodisintegration reaction

$$\lambda^*(T) = \int_0^\infty c n_\lambda^{Planck}(E,T)\sigma^*(E)dE$$

$$n_\gamma^{Planck}(E,T) = \left(\frac{1}{\pi}\right)^2\left(\frac{1}{\hbar c}\right)^3 \frac{E^2}{\exp(E/kT)-1}$$

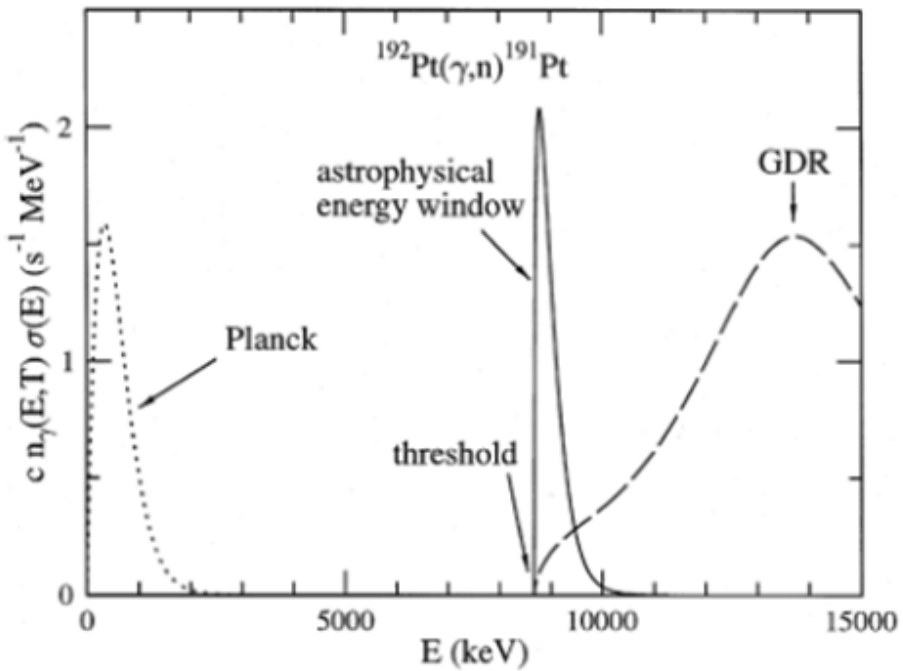

P. Mohr et al. (Phys. Lett. B 488, (2000))

A. Zilges, D.L. Balabanski, J. Isaak, N. Pietralla, Prog. Part. Nucl. Phys. **122** (2022) 103903.

Nuclear Resonance Fluorescence (NRF) Measurements on ^{78,80}Kr to determine the γSF for *p*-process nucleosynthesis calculations

No γSF data available for ^{78,80}Kr!!

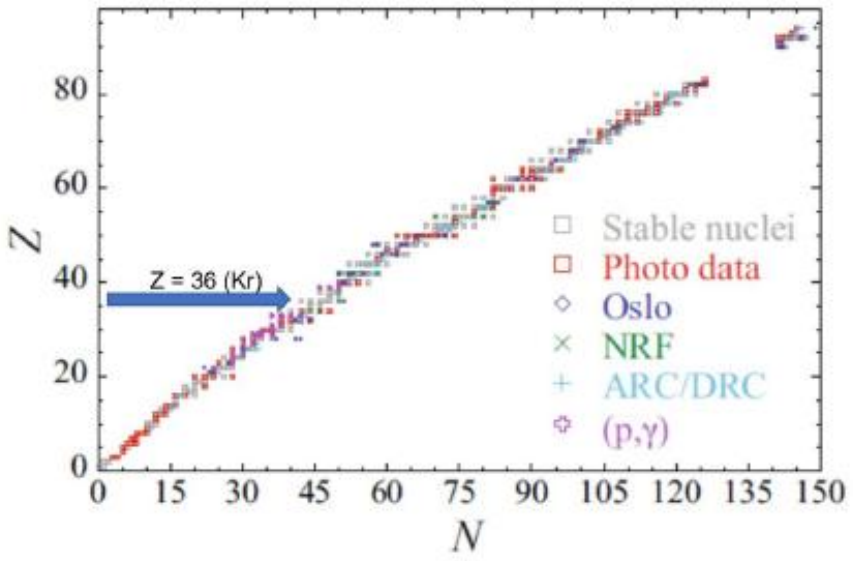

S. Goriely et al, Eur. Phys. J. A 55, 172 (2019)

PHYSICAL REVIEW C 73, 015804 (2006)

Branchings in the *γ* process path revisited

Thomas Rauscher*
Departement für Physik und Astronomie, Universität Basel, CH-4056 Basel, Switzerland

TABLE II. Nuclei with large rate uncertainties (derived from rate set A [10], see text); subscripts at each neutron number indicate which rate ($\lambda_{\gamma p}$ or $\lambda_{\gamma\alpha}$) is close to the $\lambda_{\gamma n}$ rate within factors of 3 and 10, respectively.

Z	Neutron number N at given temperature T_9		
	2.0	2.5	3.0
34	42_{α}		
35	46_{γ}	46_{γ}	
36	$44_{p,\alpha}$	44_{p}	
37		48_{p}	$45_{p}, 48_{p}$
38	43_{p}	$43_{p}, 46_{p}$	46_{p}
39	49_{p}	49_{p}	49_{p}
40	47_{p}	50_{p}	50_{p}

^{80}Kr was identified as a *key branching point*, for which the (γ,p) and (γ,α) reaction rates were found to be larger than the (γ,n) rate – NON-SMOKER calculations with GLO model for γSF & a shifted Fermi-gas model for NLD.

Contrary to NON-SMOKER calculations, TALYS calculations indicate the dominance of the ^{80}Kr(γ,n) channel over the ^{80}Kr(γ,p) and ^{80}Kr(γ,α) channels => **^{78}Kr production follows the path ^{80}Kr(γ,n)^{79}Kr(γ,n)^{78}Kr**

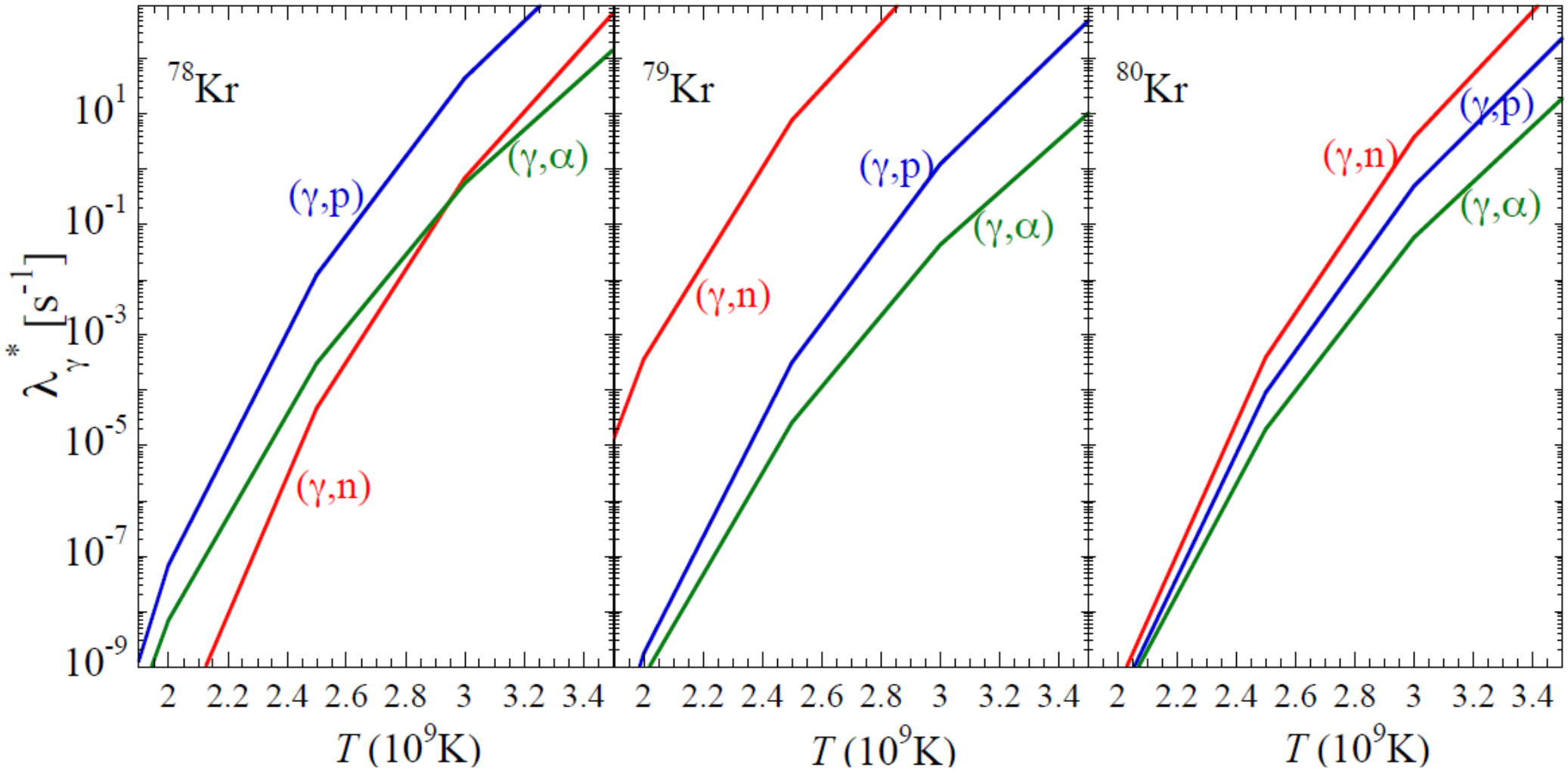

TALYS calculations with the **D1M+QRPA γSF model** and HFB plus combinatorial NLD model

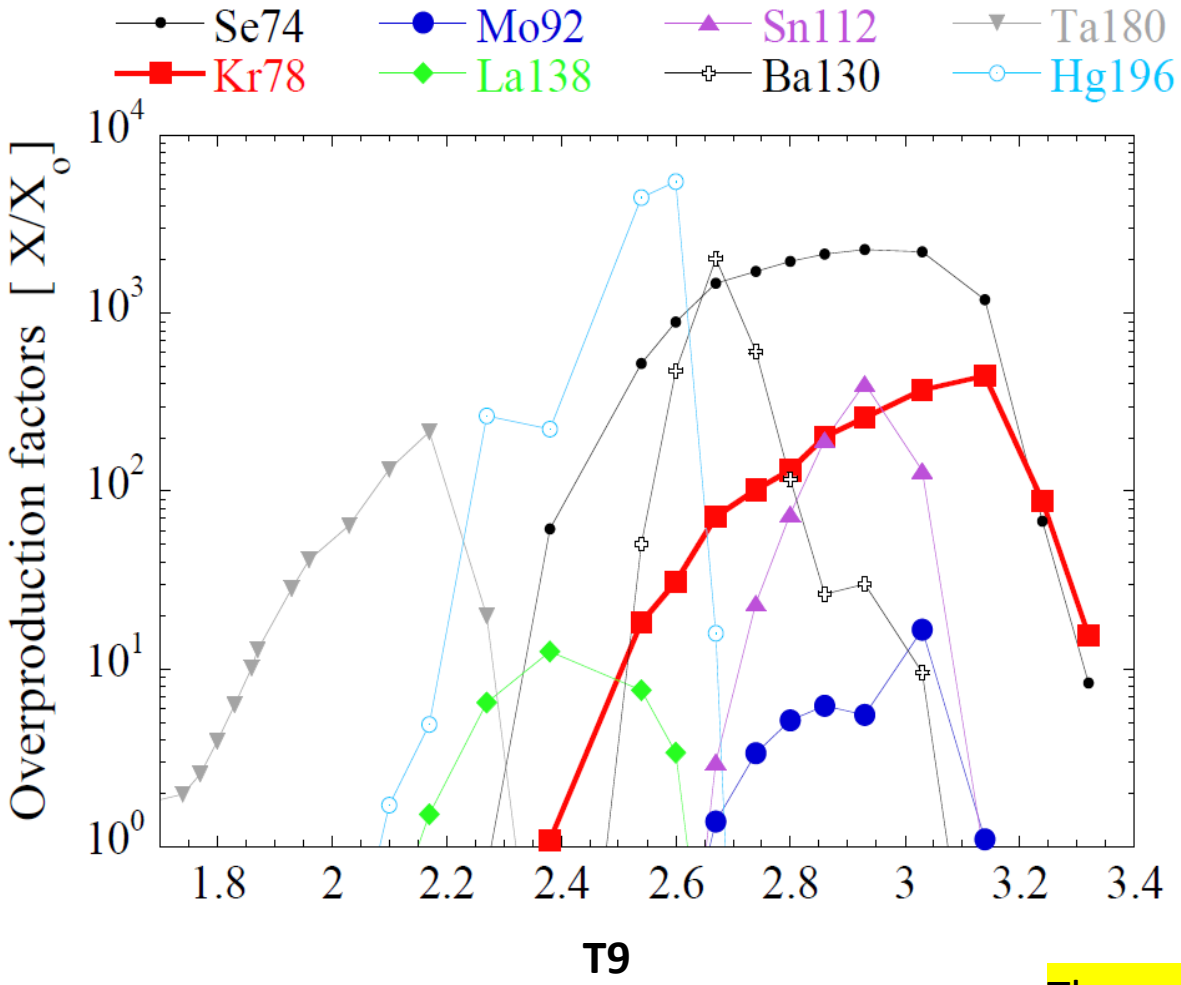

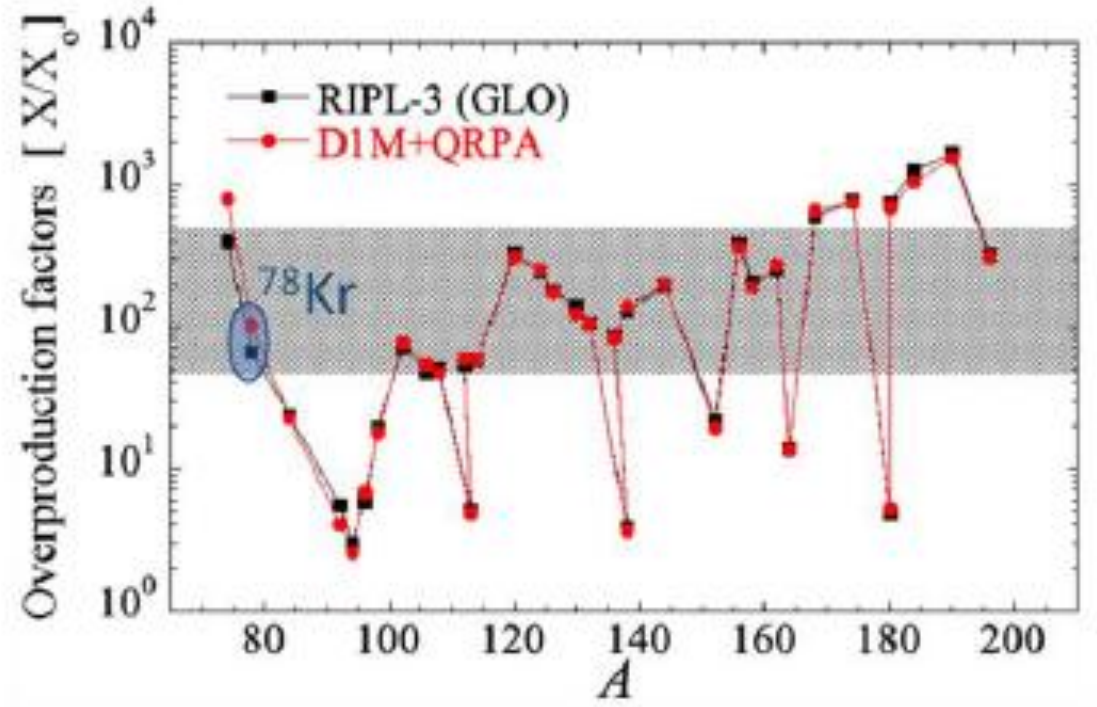

The production of the ^{78}Kr via the path ^{80}Kr(γ,n)^{79}Kr(γ,n)^{78}Kr is increased by 54%, while the (γ,n) destruction of ^{80}Kr is increased by a factor of 2.6 at T = 3 GK **when using the D1M+QRPA γSf model comparative to the GLO γSF model**.

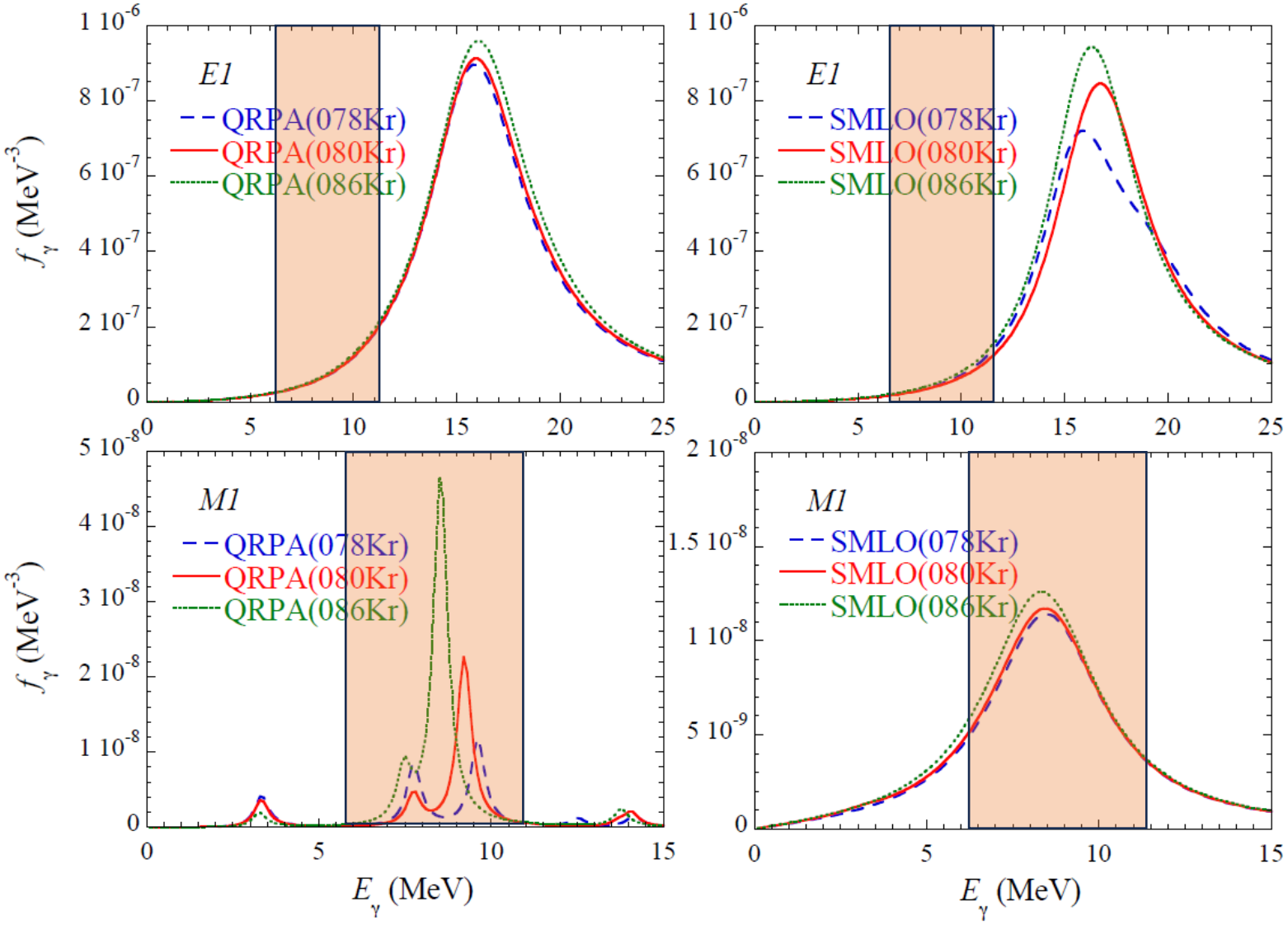

Photon Beam Energies (MeV) for our NRF measurements:

6.40, 6.65, 6.95, 7.20, 7.28, 7.50, 7.80, 8.15, 8.45, 8.80, 8.92, 9.15, 9.55, 9.95, 10.35, 10.75, 11.20

$S_n(^{78}Kr)$ = 12.1 MeV

$S_n(^{80}Kr)$ = 11.5 MeV

CONCEPT OF PHOTON STRENGTH FUNCTIONS

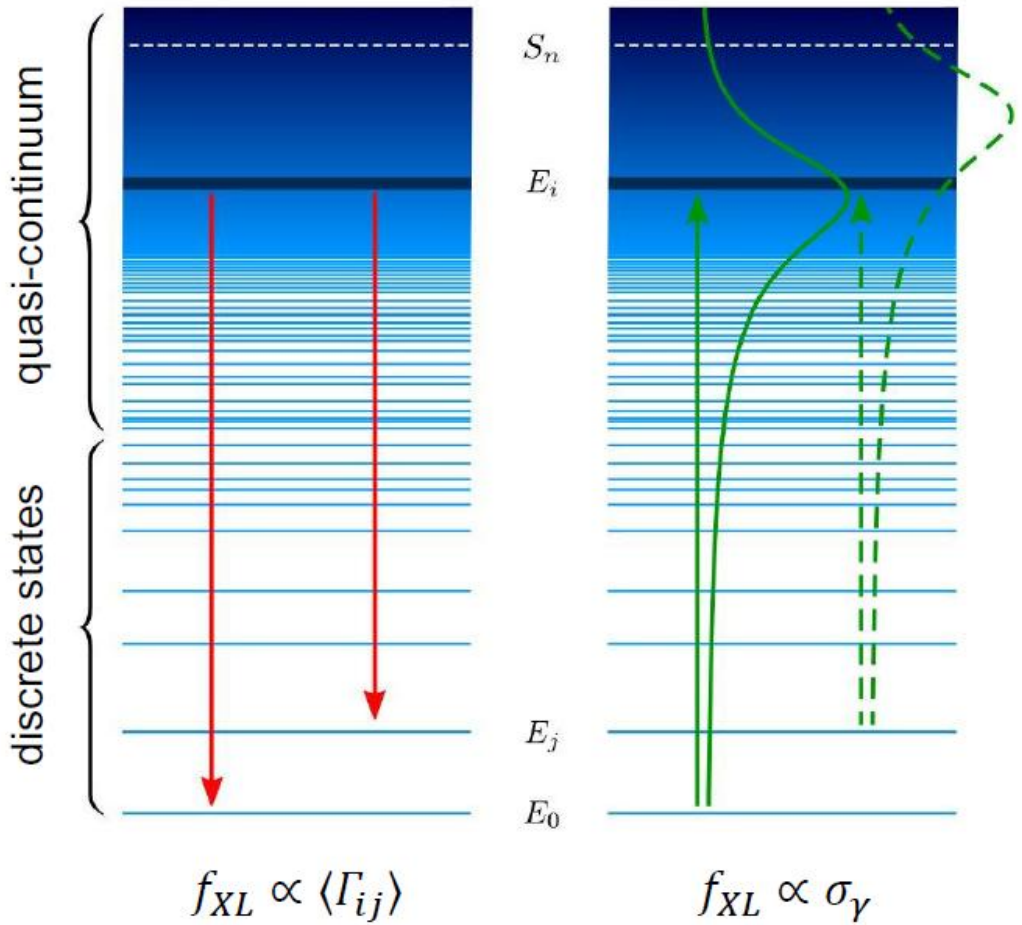

$$\sigma_\gamma = \sigma_{\gamma\gamma} + \sigma_{\gamma\gamma'} \quad \rightarrow \quad f(E_\gamma) = \frac{1}{3(\pi\hbar c)^2} \cdot \frac{\sigma_\gamma}{E_\gamma}$$

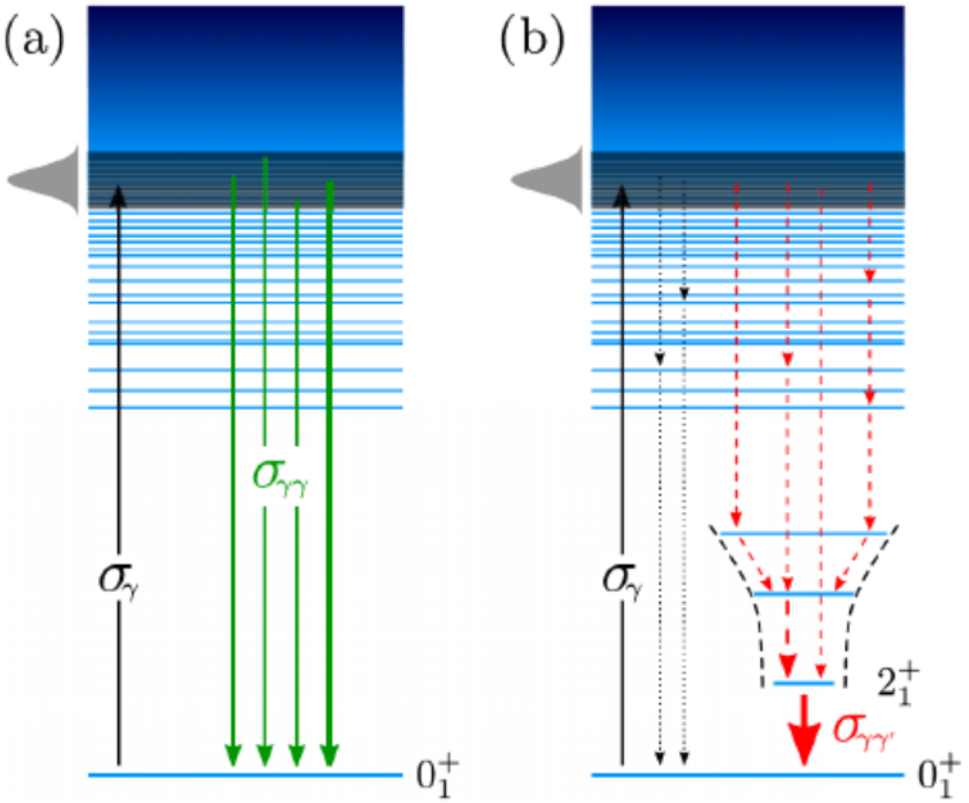

Credits: J. Isaak

High Intensity Gamma-ray Source (HIGS) at TUNL

- Highest intensity (γ-rays/s/keV) γ-ray beam in the world
- Produces γ-rays by Compton backscattering inside the optical cavity of a storage-ring FEL
- Produces both linearly and circularly polarized beams

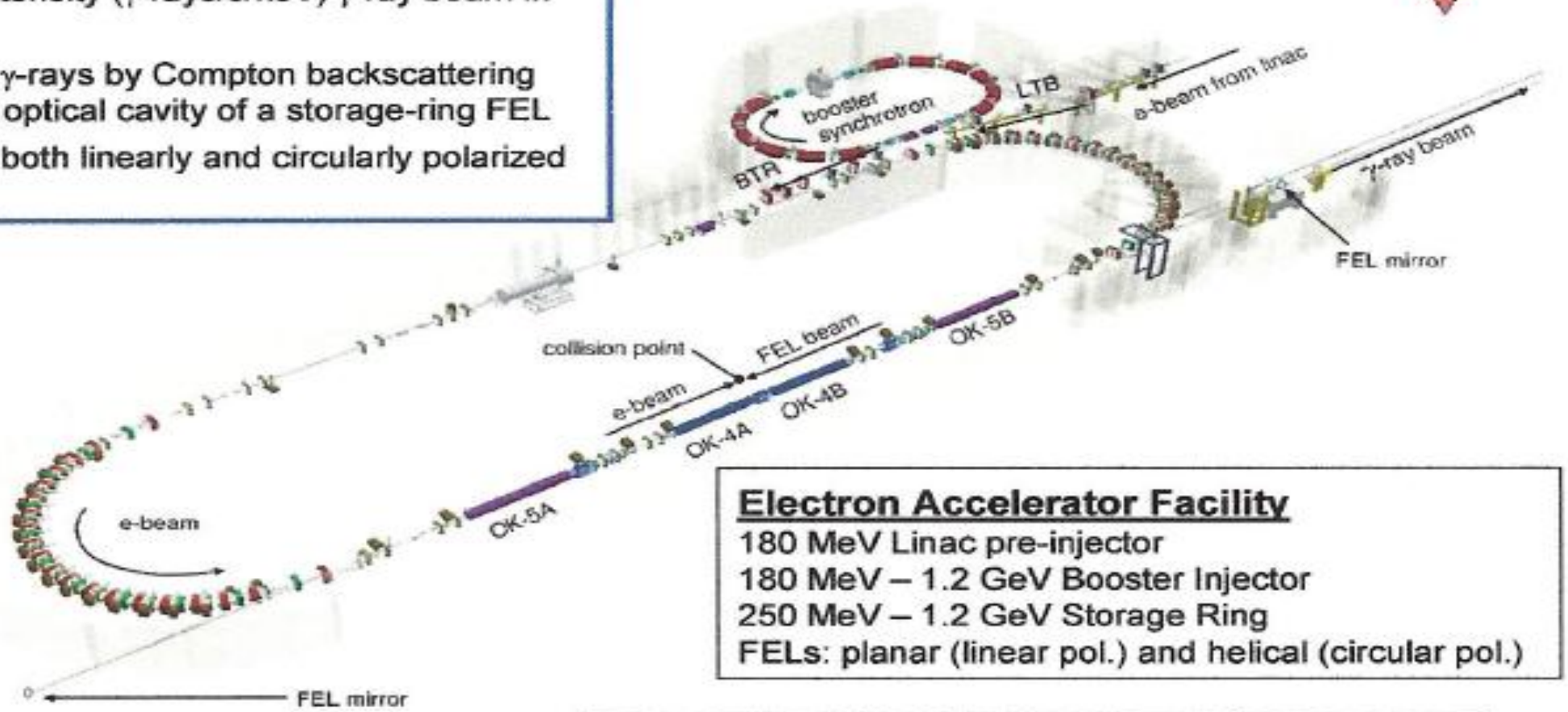

Electron Accelerator Facility

180 MeV Linac pre-injector
180 MeV – 1.2 GeV Booster Injector
250 MeV – 1.2 GeV Storage Ring
FELs: planar (linear pol.) and helical (circular pol.)

γ-ray beam parameters	Values
Energy	1 – 100 MeV
Linear & circular polarization	> 95%
Intensity with 5% $\Delta E_\gamma/E_\gamma$	> 10^7 γ/s

For more details see:
http://www.tunl.duke.edu/higs/

NRF Experimental Setup at HγGS

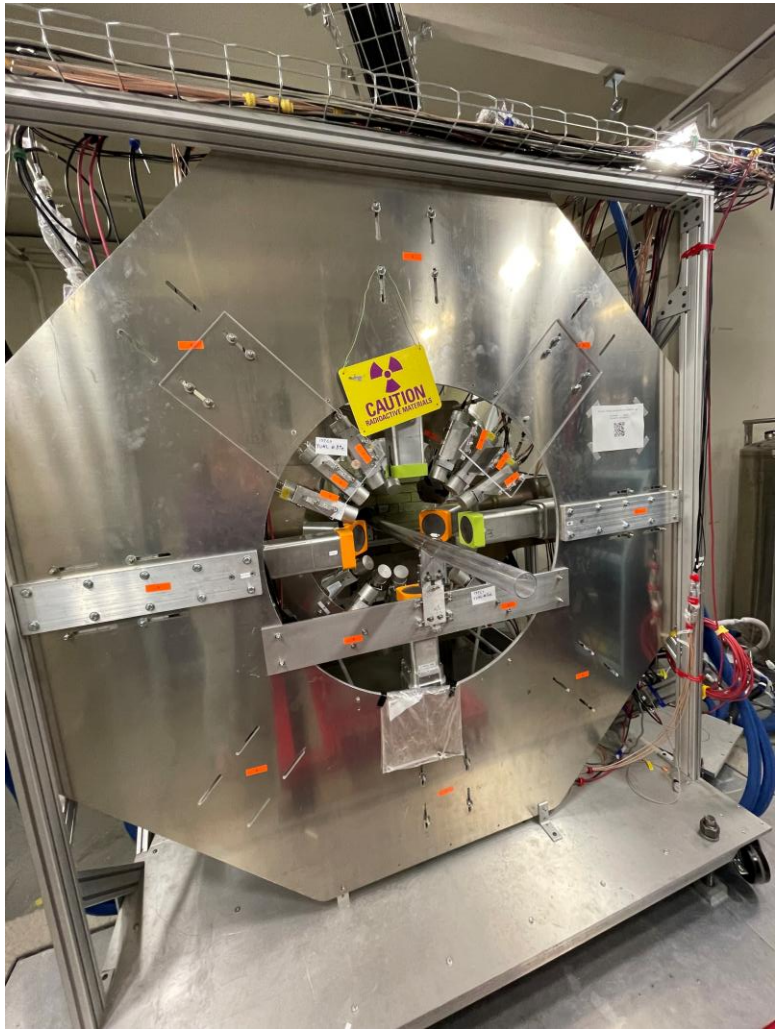

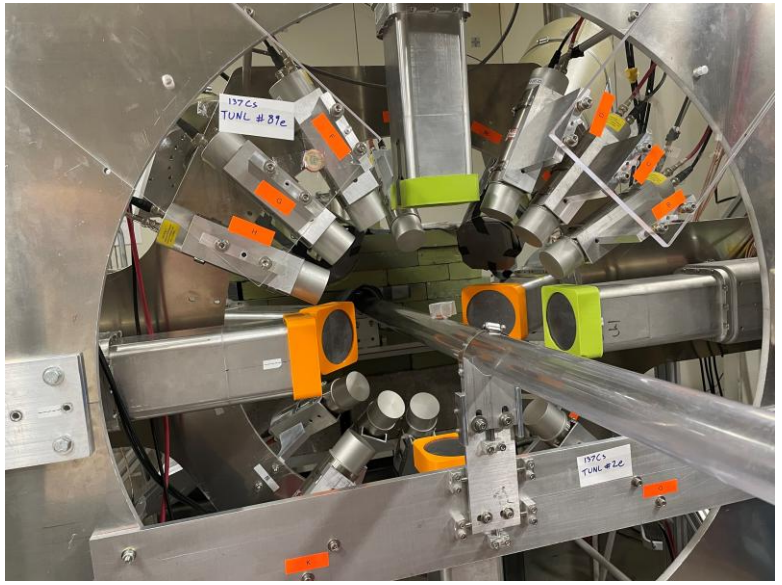

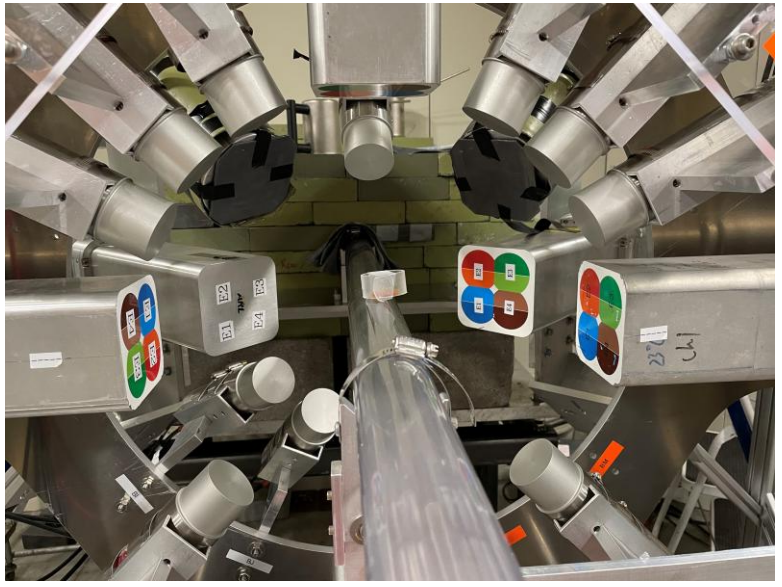

Clover array

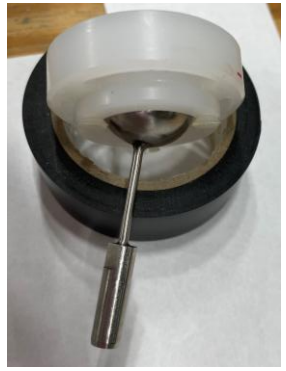

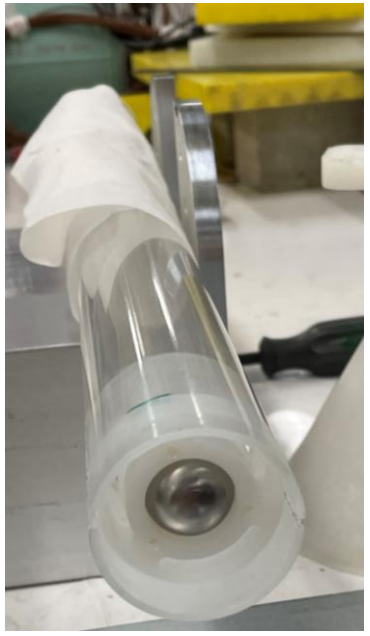

Target gas cell and target holder

Photon beam flux measurements

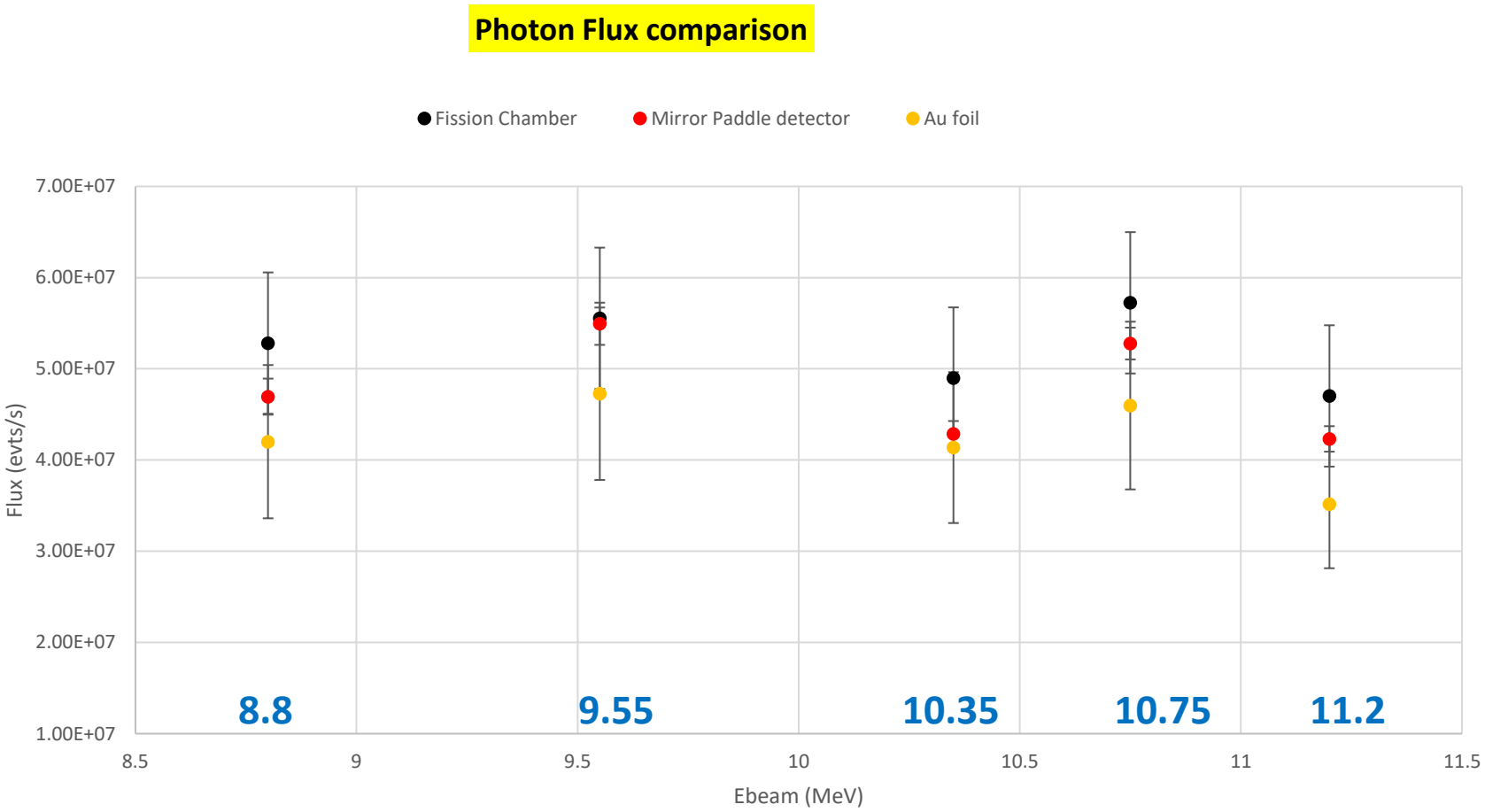

Photon Beam Energies (MeV) for our NRF measurements:

6.40, 6.65, 6.95, 7.20, 7.28, 7.50, 7.80, 8.15, 8.45, **8.80**, 8.92, 9.15, **9.55**, 9.95, **10.35, 10.75, 11.20**

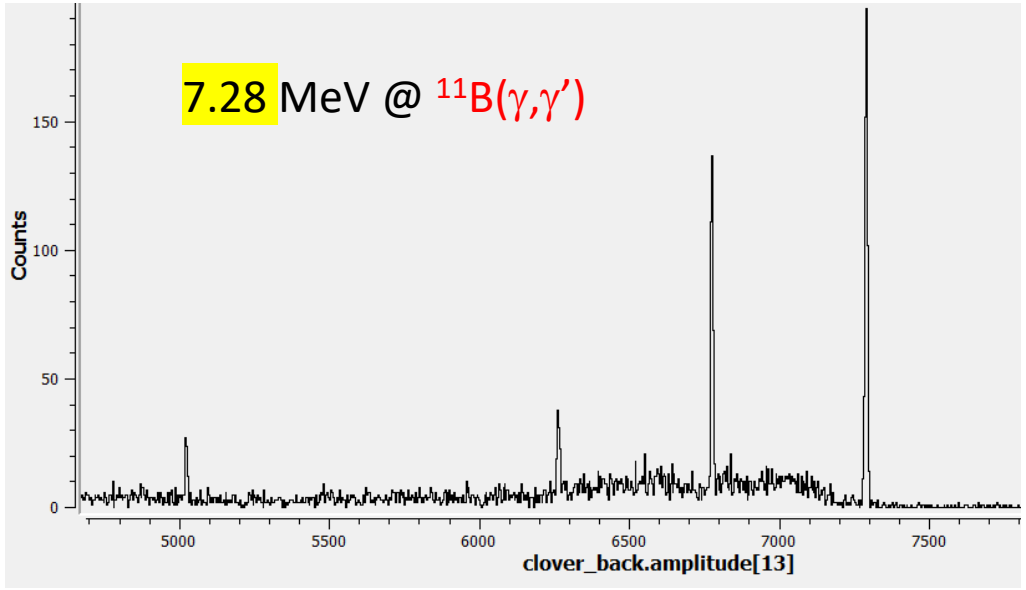

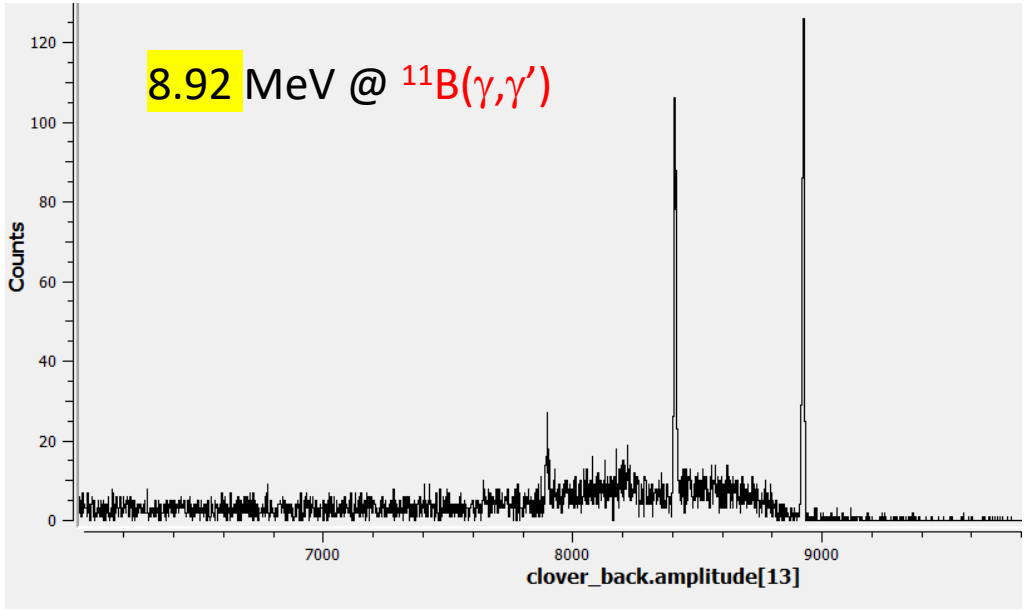

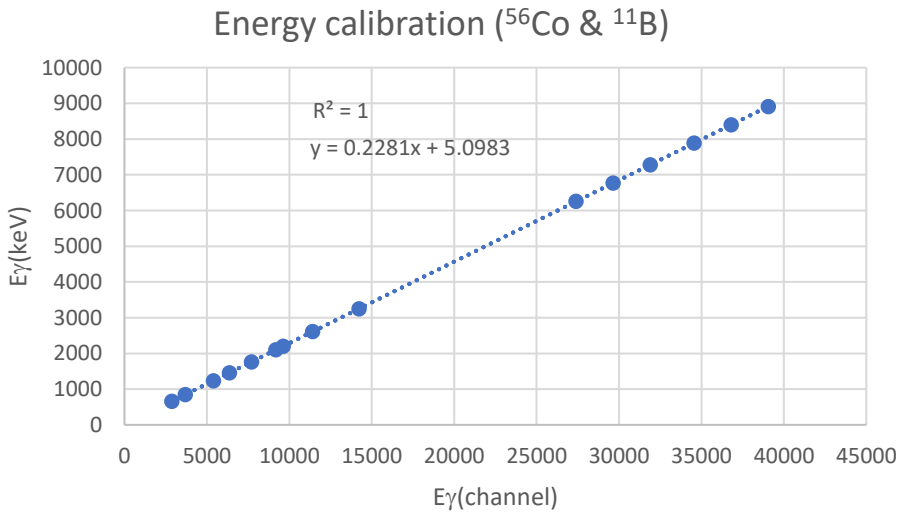

^{80}Kr NRF measurements (2023)

6.4 MeV @ ^{56,54}Fe(γ,γ') & **^{80}Kr(γ,γ')**

target: stainless-steel cell with **^{80}Kr**

$$\Delta E_\gamma / E_\gamma \sim 4\%$$

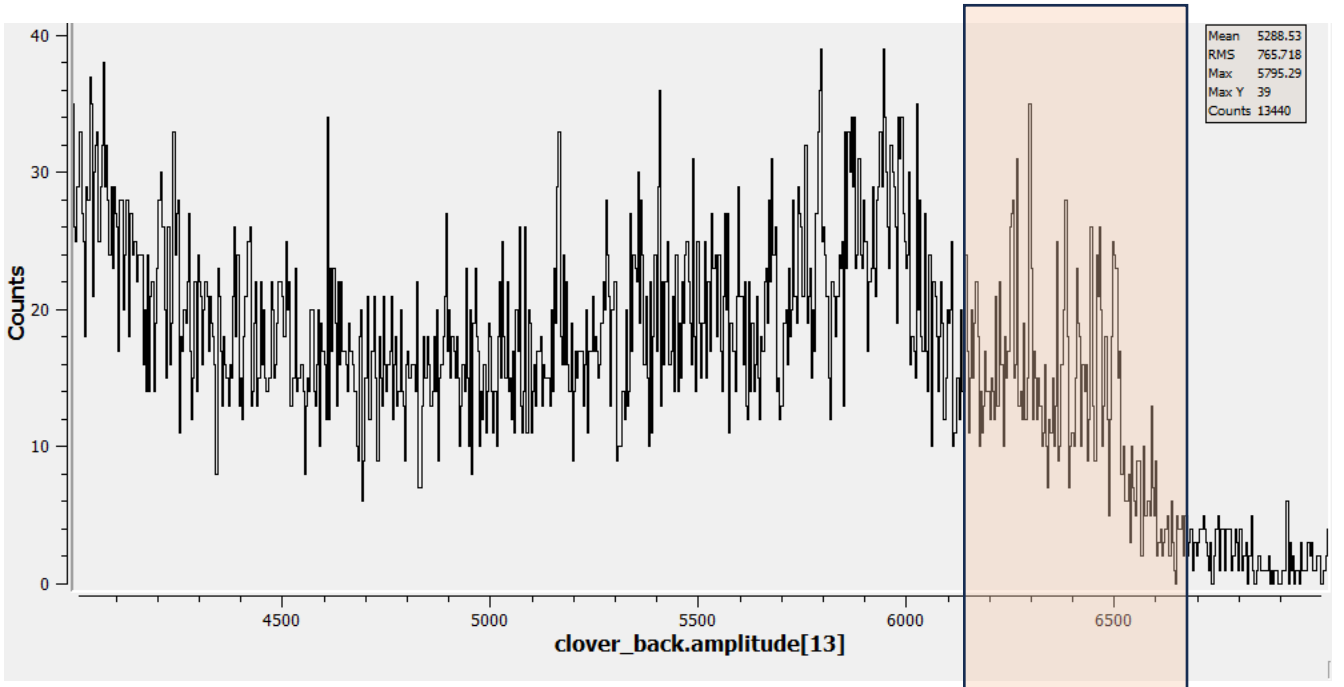

6.4 MeV @ ^{56,54}Fe(γ,γ')

target: stainless-steel **empty cell**

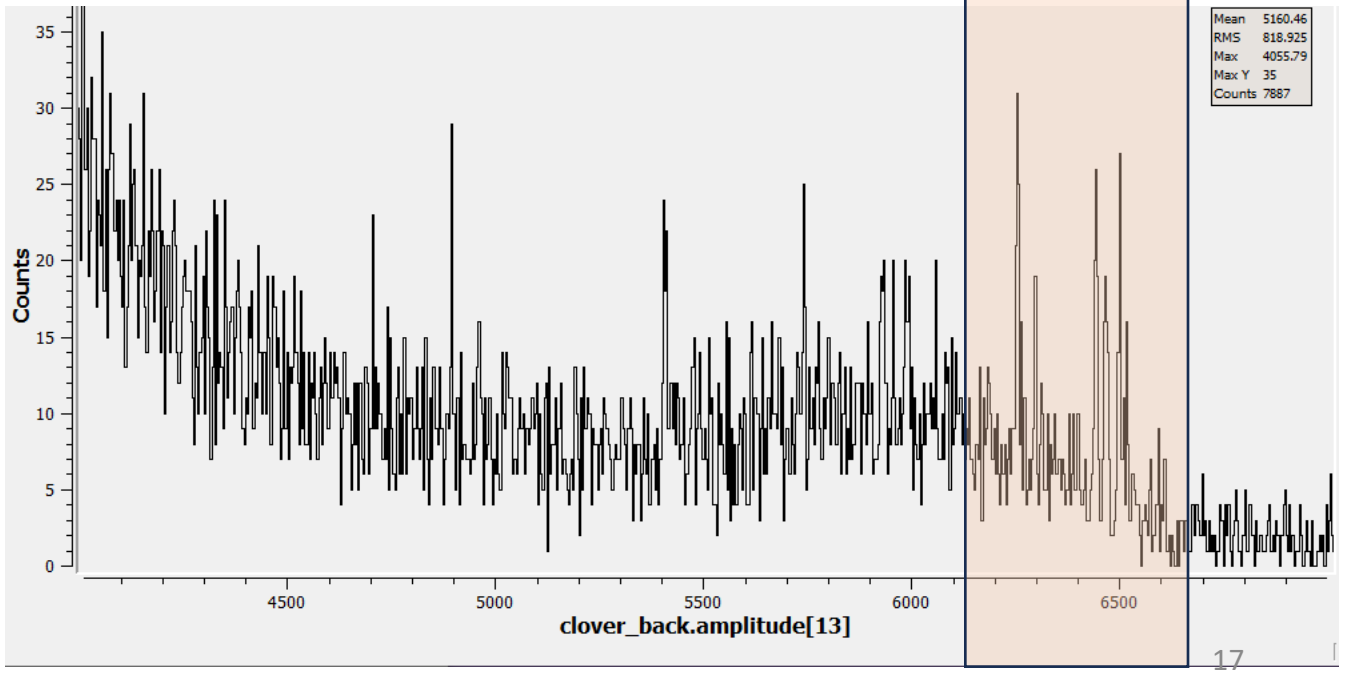

Data analysis in progress

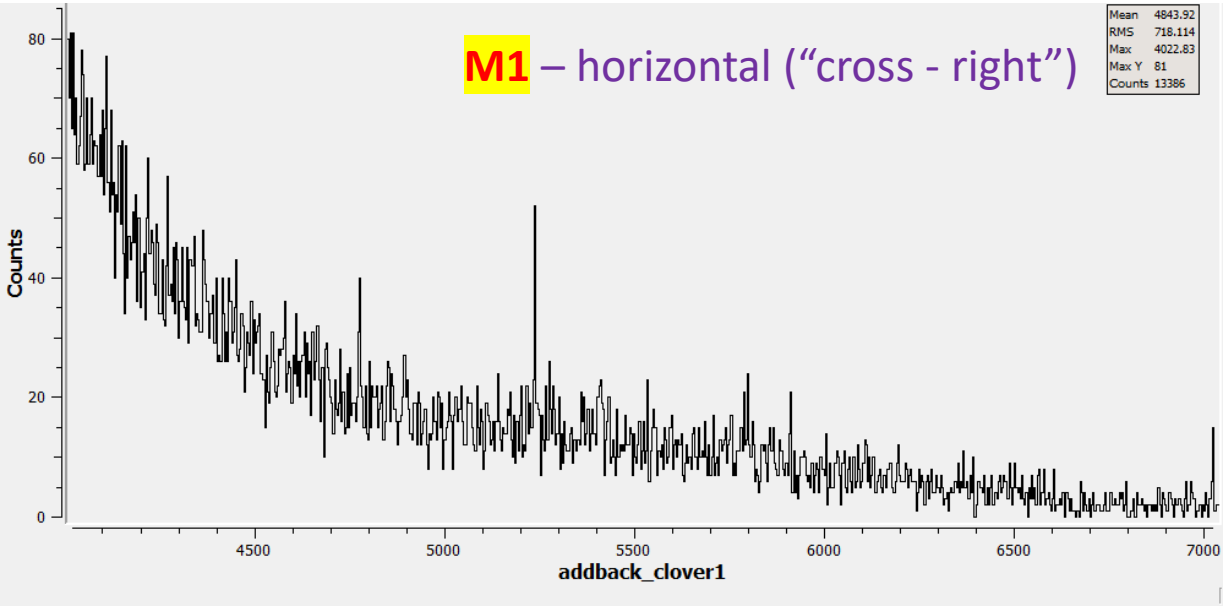

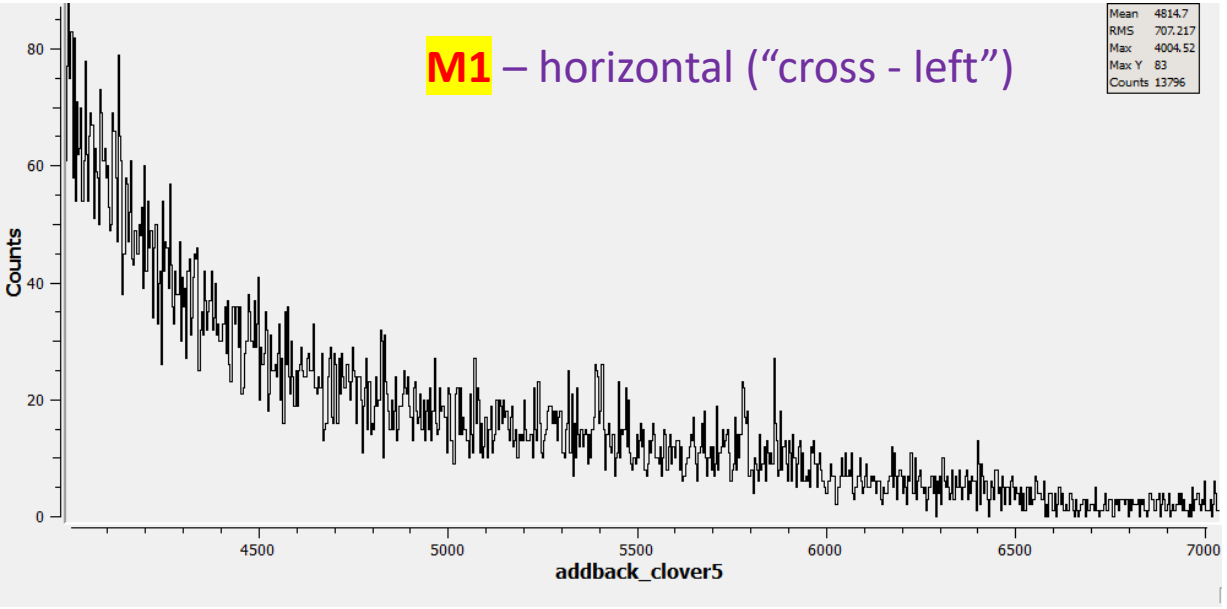

6.4 MeV @ ^{56,54}Fe(γ,γ’) & ^{80}Kr(γ,γ’)

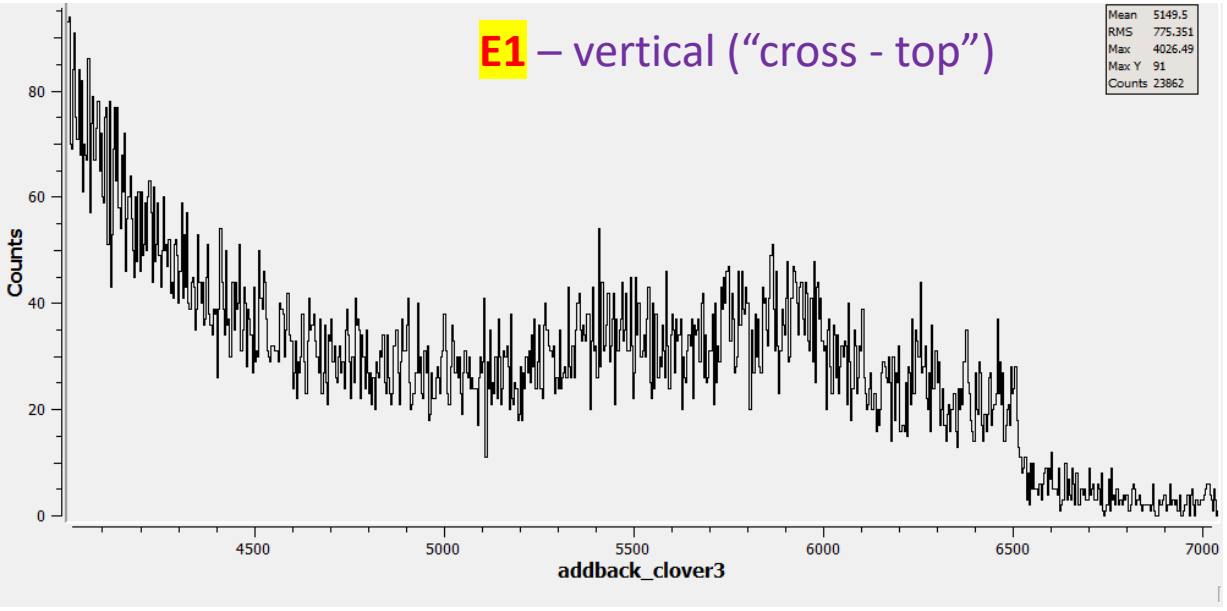

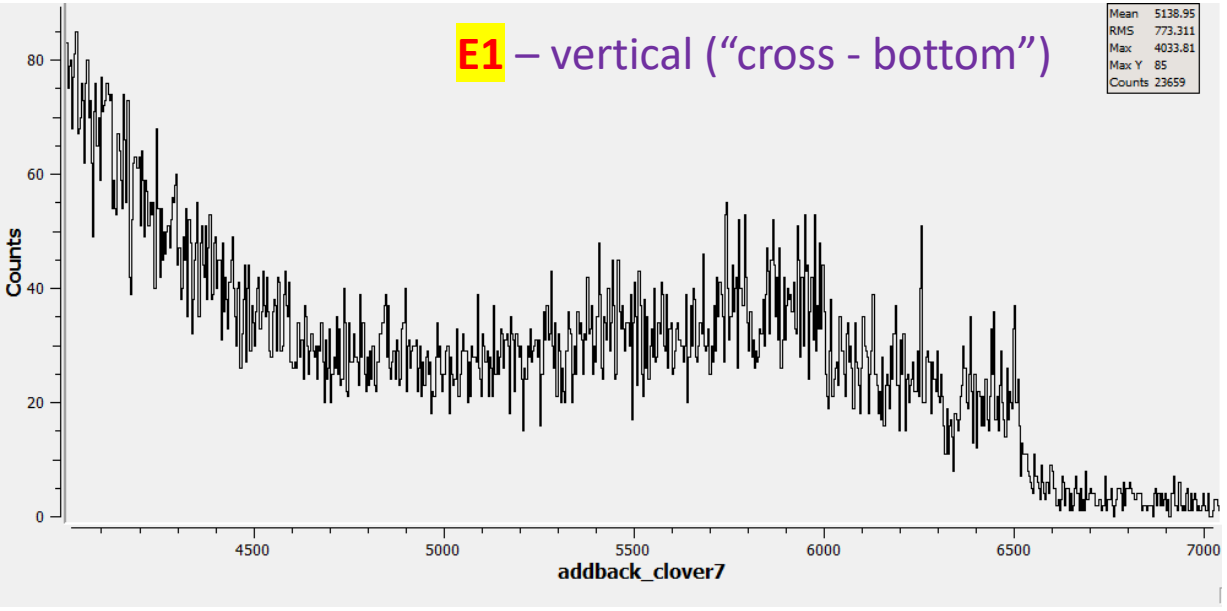

Data analysis in progress

^{80}Kr NRF measurements

11.2 MeV @ ^{56,54}Fe(γ,γ') & **^{80}Kr(γ,γ')**

target: stainless-steel cell with **^{80}Kr**

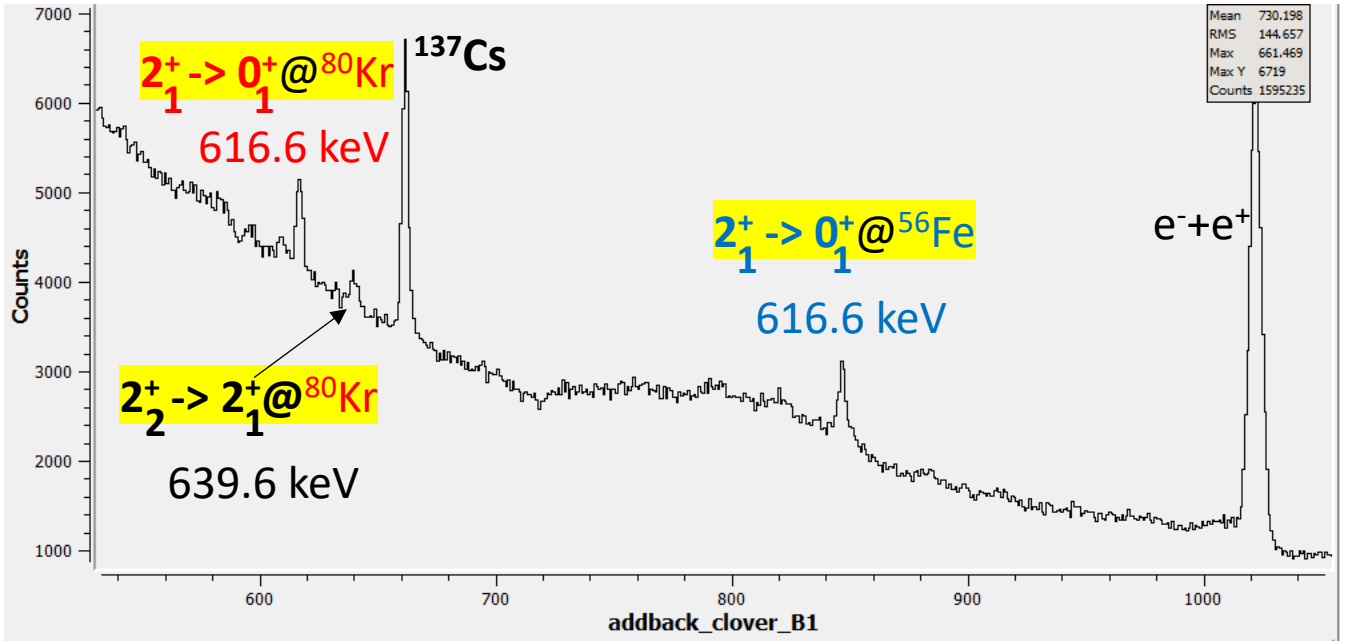

Data analysis in progress

Photoneutron reaction cross section measurements on ^{94}Mo and ^{90}Zr relevant to the *p*-process nucleosynthesis

A. Banu* and E. G. Meekins†
Department of Physics and Astronomy, James Madison University, Harrisonburg, Virginia 22807, USA

J. A. Silano‡ and H. J. Karwowski
Triangle Universities Nuclear Laboratory, Durham, North Carolina 27708, USA
and University of North Carolina at Chapel Hill, Chapel Hill, North Carolina 27516, USA

S. Goriely
Institut d'Astronomie et d'Astrophysique, Université Libre de Bruxelles, Campus de la Plaine, CP-226, 1050 Brussels, Belgium

(Received 10 June 2018; revised manuscript received 19 December 2018; published 11 February 2019)

The photodisintegration cross sections for the ^{94}Mo(γ, n) and ^{90}Zr(γ, n) reactions have been experimentally investigated with quasi-monochromatic photon beams at the High Intensity γ-ray Source (HIγS) facility of the Triangle Universities Nuclear Laboratory (TUNL). The energy dependence of the photoneutron reaction cross sections was measured with high precision from the respective neutron emission thresholds up to 13.5 MeV. These measurements contribute to a broader investigation of nuclear reactions relevant to the understanding of the *p*-process nucleosynthesis. The results are compared with the predictions of Hauser-Feshbach statistical model calculations using two different models for the dipole γ-ray strength function. The resulting ^{94}Mo(γ, n) and ^{90}Zr(γ, n) photoneutron stellar reaction rates as a function of temperature in the typical range of interest for the *p*-process nucleosynthesis show how sensitive the photoneutron stellar reaction rate can be to the experimental data in the vicinity of the neutron threshold.

Experimental Setup

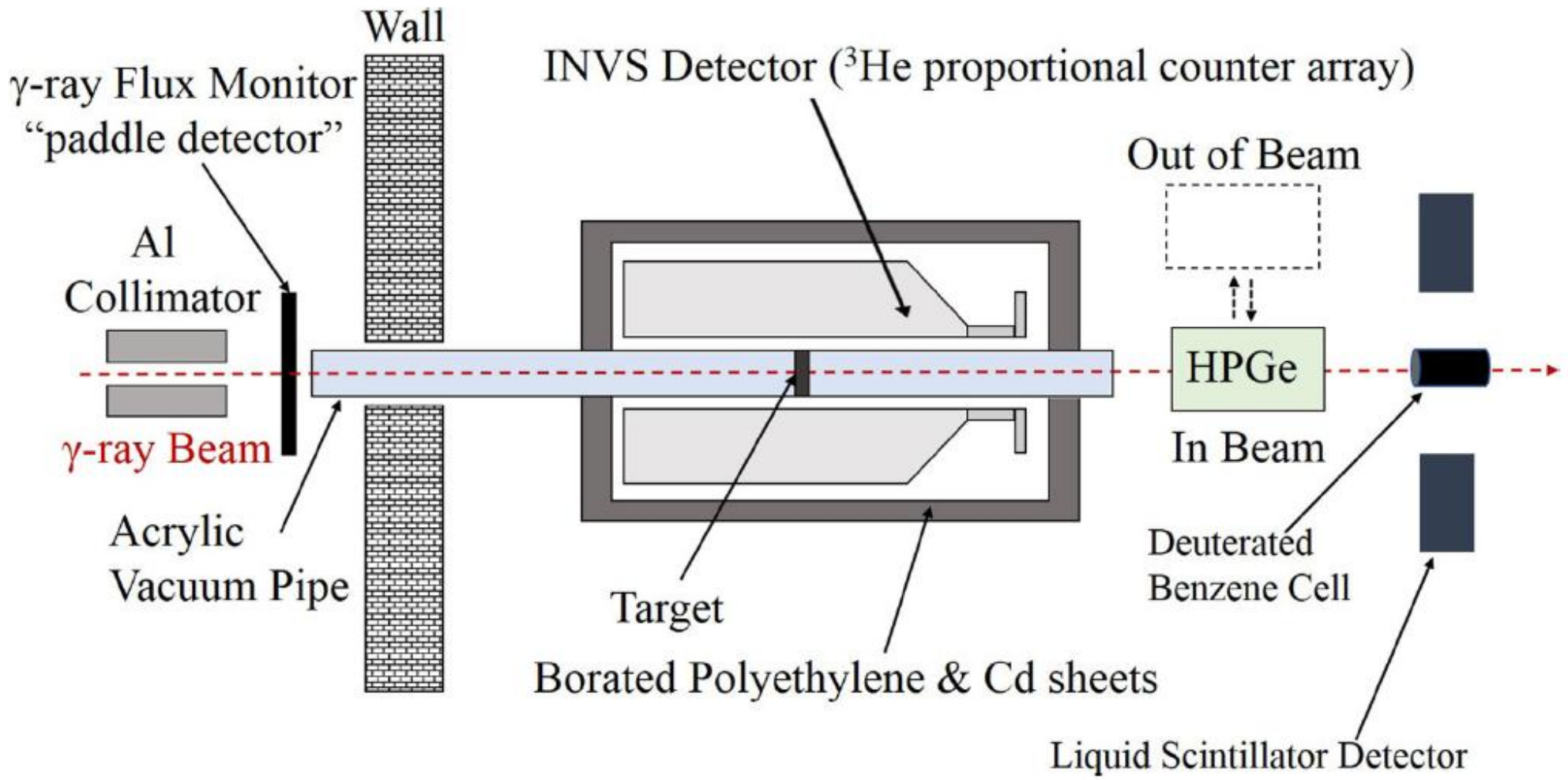

~ 10^7 – 10^8 γ/s

- **^{94}Mo: ~ 600 mg/cm^2, 98.97%**
- **^{90}Zr: ~ 1 g/cm^2, 97.7%**

$\Delta E_\gamma / E_\gamma \sim 4\% - 5\%$

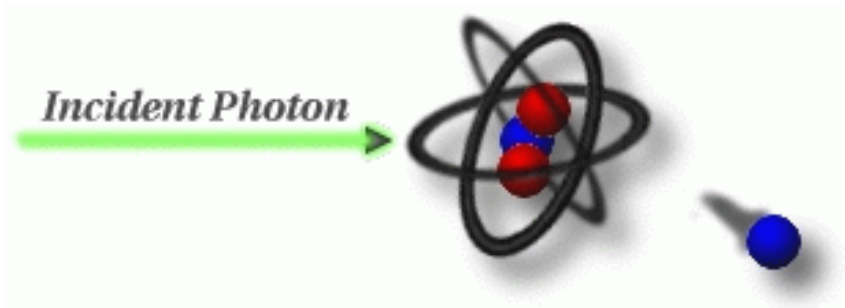

$$\gamma + {}^{90}Zr \rightarrow {}^{90}Zr^{*} \rightarrow {}^{89}Zr + n$$

γ-ray Beam Energies (MeV):

12, 12.1, 12.2, 12.4, 12.5, 12.8, 13, 13.5

(only g.s. neutrons) (g.s./excited-state neutrons)

$$\sigma(E_\gamma) = \frac{N_n}{N_\gamma N_t \varepsilon_n(E_\gamma)}$$

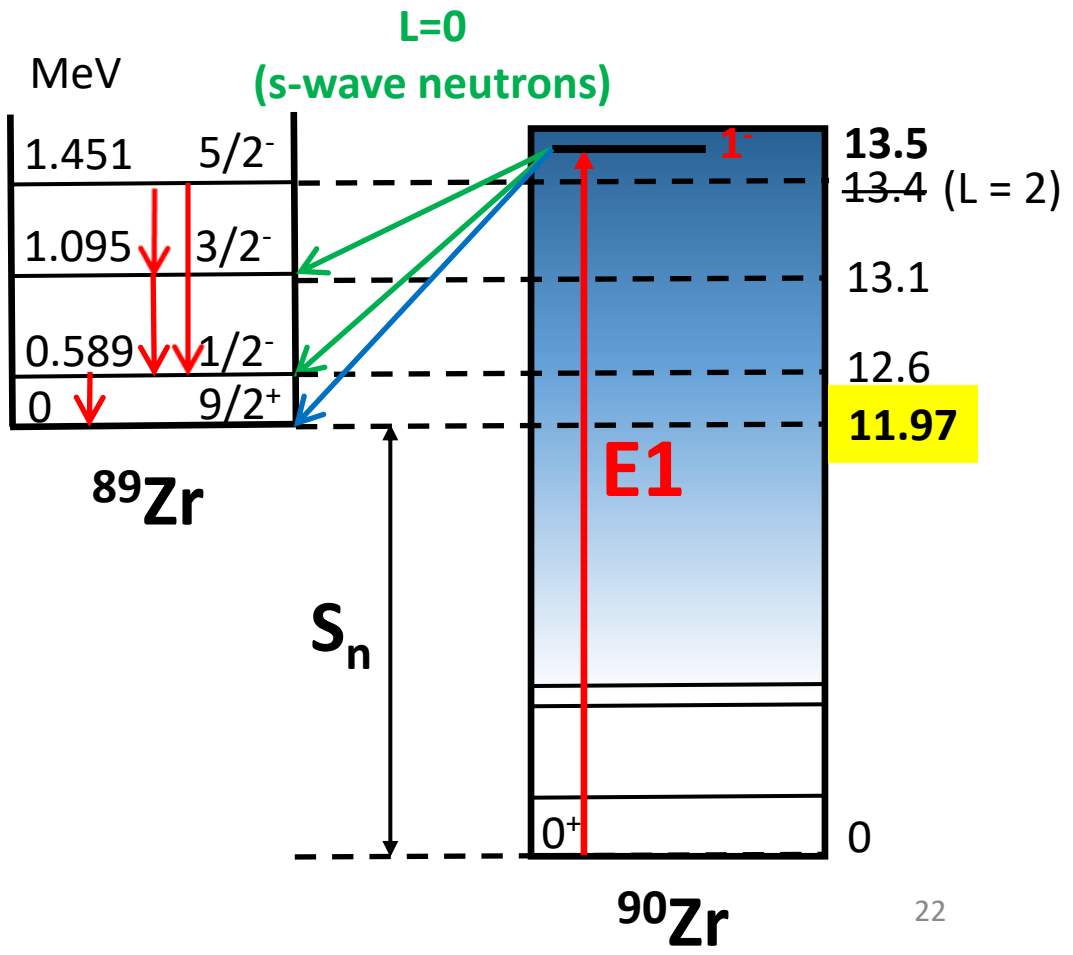

N_n – number of neutrons detected using ^{3}He counters

N_γ - number of incident photons

N_t – number of target atoms per unit area (enriched target)

ε_n – neutron detection efficiency

Neutron Detection Efficiency

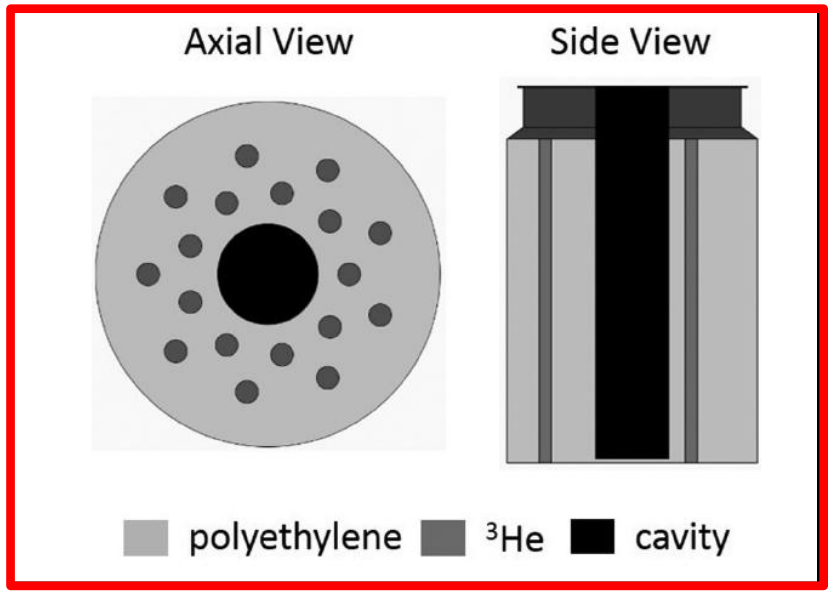

C. W. Arnold et al., Nucl. Instr. and Meth. A 647, 55 (2011)

Neutron energy is lost by the **thermalization** of neutrons in the moderator (polyethylene)!!

- Simulated efficiencies for neutron energies of interest:

~55% @ 20 keV - ~25% @ 4 MeV

$$E_{n0} = \left(\frac{A-1}{A}\right)(E_\gamma - S_n)$$ (for g.s. neutrons)

$$E_{ni} = \left(\frac{A-1}{A}\right)(E_\gamma - S_n - E_i)$$ (for excited-state neutrons)

$\varepsilon_{ni}(E_{ni})$ – neutron efficiency from Geant4 simulations

b_i – neutron branching from TALYS calculations

Effective neutron efficiency:

$$\epsilon_n^{\text{eff}} = \sum_i b_i \epsilon_{n_i}(E_{n_i})$$

Nuclear Instruments and Methods in Physics Research A 647 (2011) 55–62

Contents lists available at ScienceDirect

Nuclear Instruments and Methods in Physics Research A

journal homepage: www.elsevier.com/locate/nima

Characterization of an INVS model IV neutron counter for high precision (γ,n) cross-section measurements

C.W. Arnold [a,b,*], T.B. Clegg [a,b], H.J. Karwowski [a,b], G.C. Rich [a,b], J.R. Tompkins [a,b], C.R. Howell [b,c]

[a] Department of Physics and Astronomy, University of North Carolina at Chapel Hill, Chapel Hill, NC 27599, United States
[b] Triangle Universities Nuclear Laboratory (TUNL), Durham, NC 27708, United States[1]
[c] Department of Physics, Duke University, Durham, NC 27708, United States

ARTICLE INFO

Article history:
Received 18 October 2010
Received in revised form
17 January 2011
Accepted 21 January 2011
Available online 24 February 2011

Keyword:
Nuetron detector

ABSTRACT

A neutron counter designed for assay of radioactive materials has been adapted for beam experiments at TUNL. The cylindrical geometry and 60% maximum efficiency make it well suited for (γ,n) cross-section measurements near the neutron emission threshold. A high precision characterization of the counter has been made using neutrons from several sources. Using a combination of measurements and simulations, the absolute detection efficiency of the neutron counter was determined to an accuracy of ±3% in the neutron energy range between 0.1 and 1 MeV. It is shown that this efficiency characterization is generally valid for a wide range of targets.

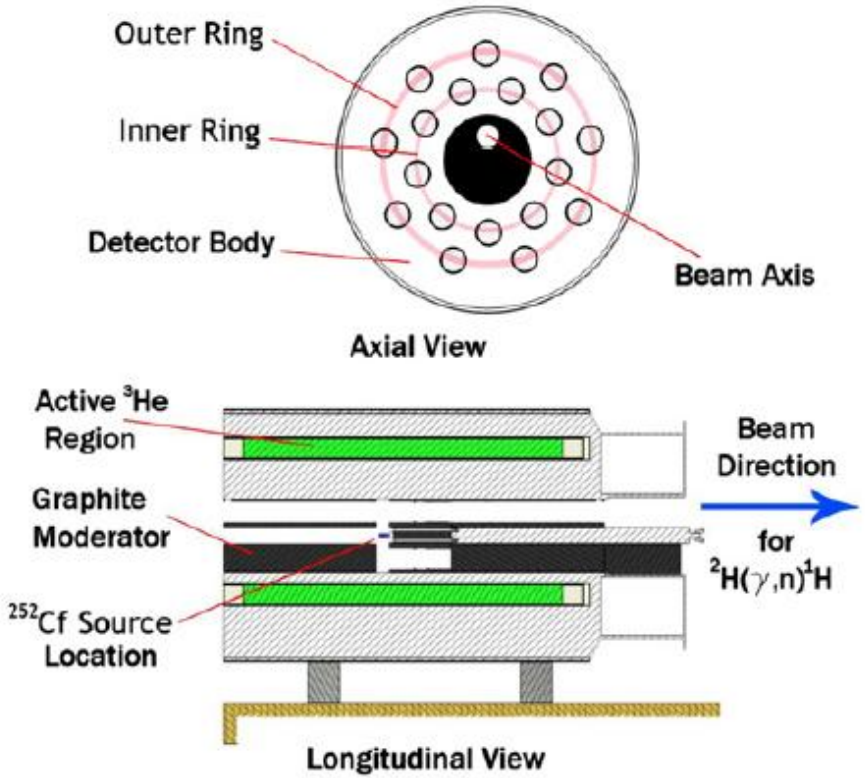

Fig. 1. Front and side cut-away cross-sectional views of the Model IV INVS counter described in the text. The arrangement of inter-cavity moderator corresponds to the experimental geometries either for the ^{252}Cf source measurement, or for the ^{2}H(γ,n)^{1}H experiment.

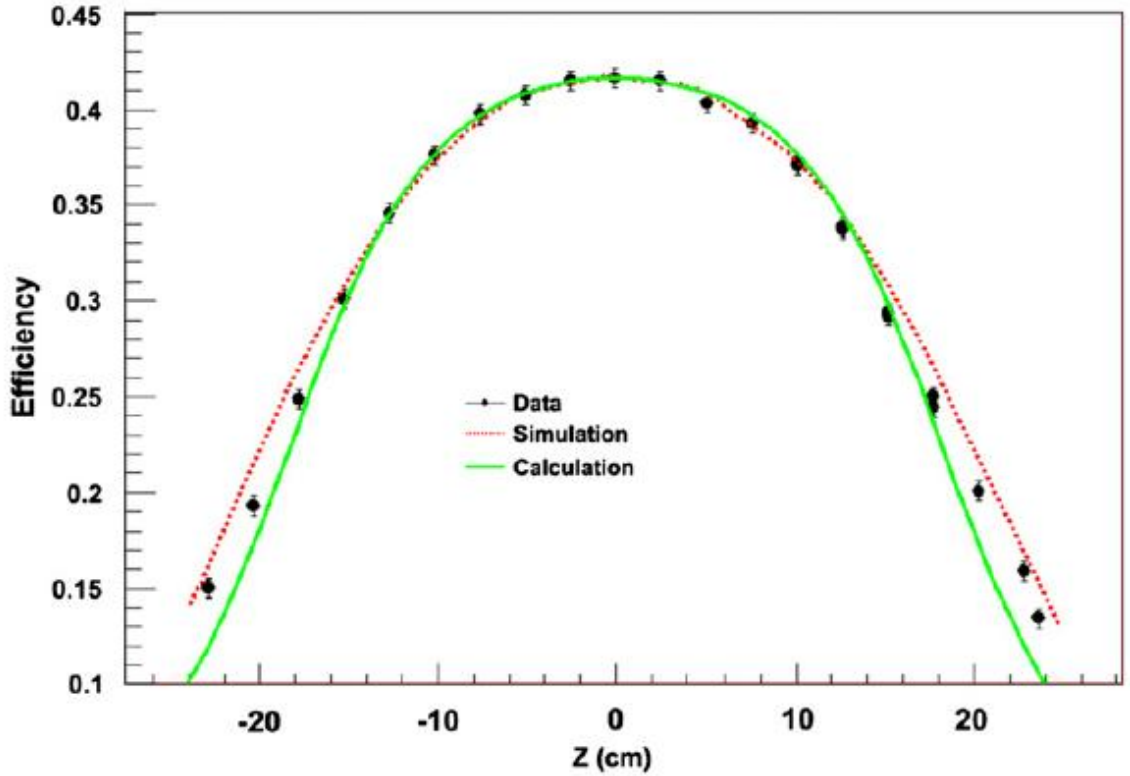

Fig. 2. Efficiency vs. *Z*-axis position for an open detector geometry.

source provides a single measurement of efficiency representing the response of the detector to a broad spectrum of neutron

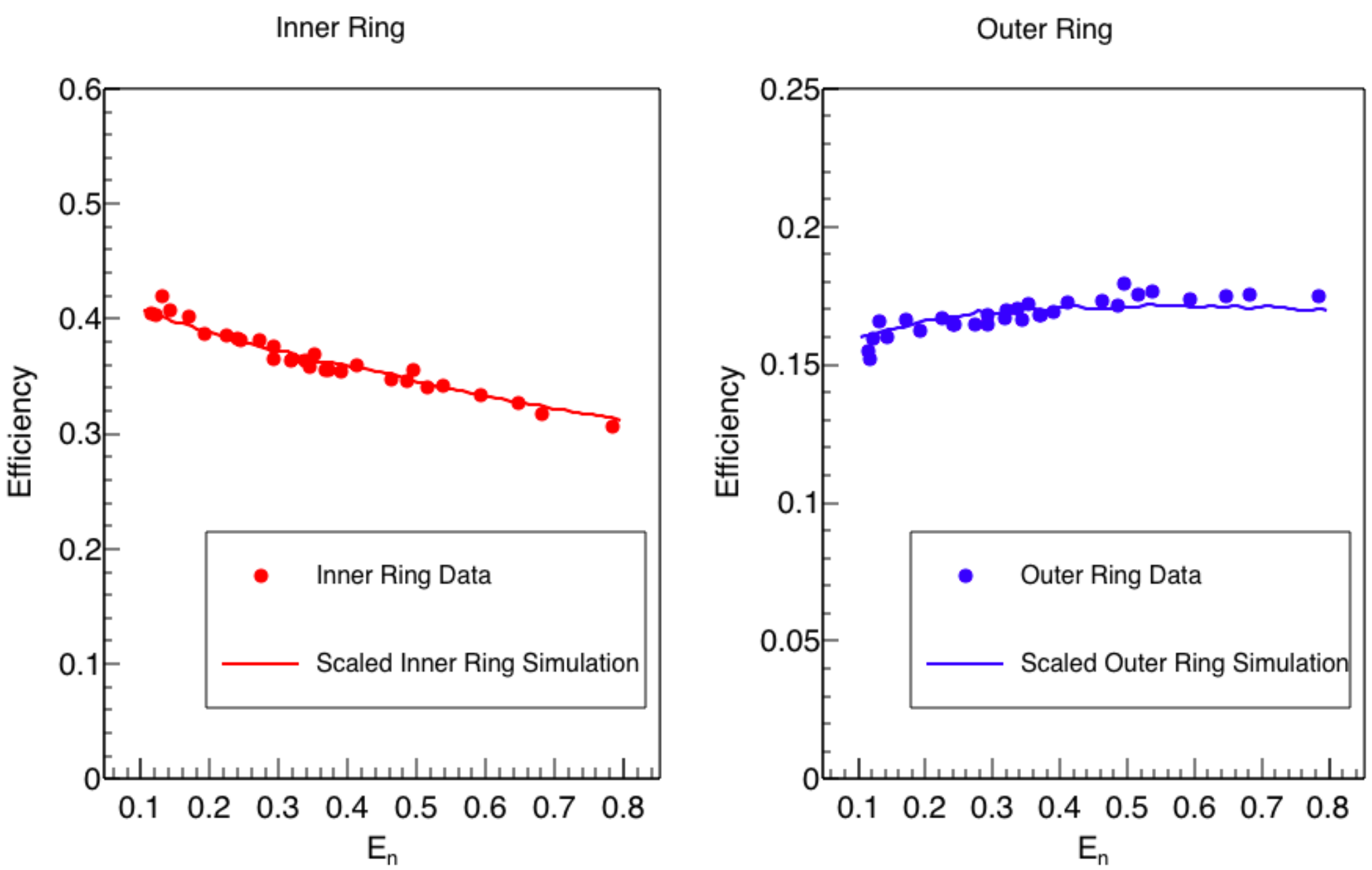

C. Arnold *et al.*, Nucl. Instrum. Methods Phys. Res. Sect. A 647,55 (2011)

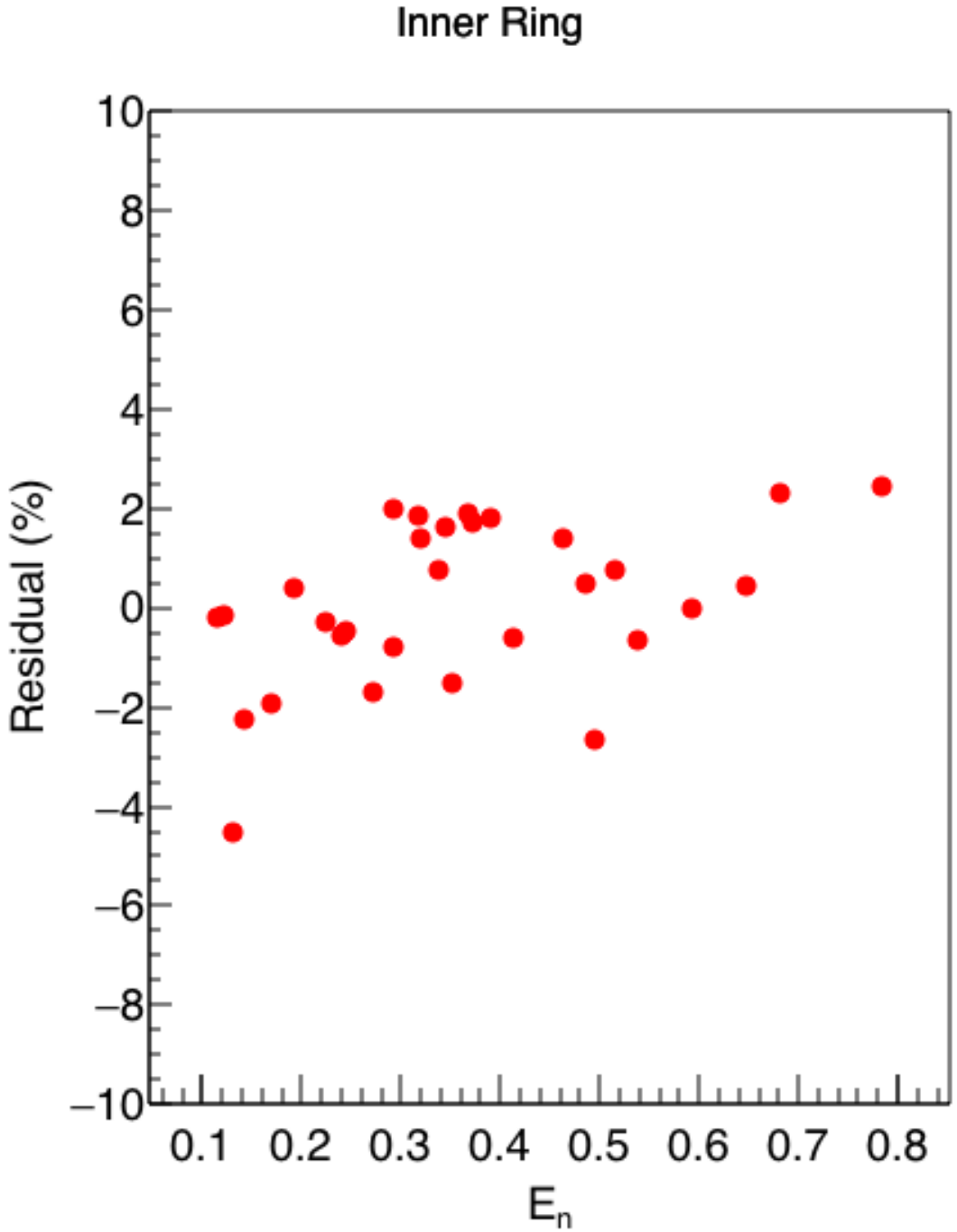
Inner Ring
Residual (%)
10
8
6
4
2
0
−2
−4
−6
−8
−10
0.1
0.2
0.3
0.4
0.5
0.6
0.7
0.8
E_n

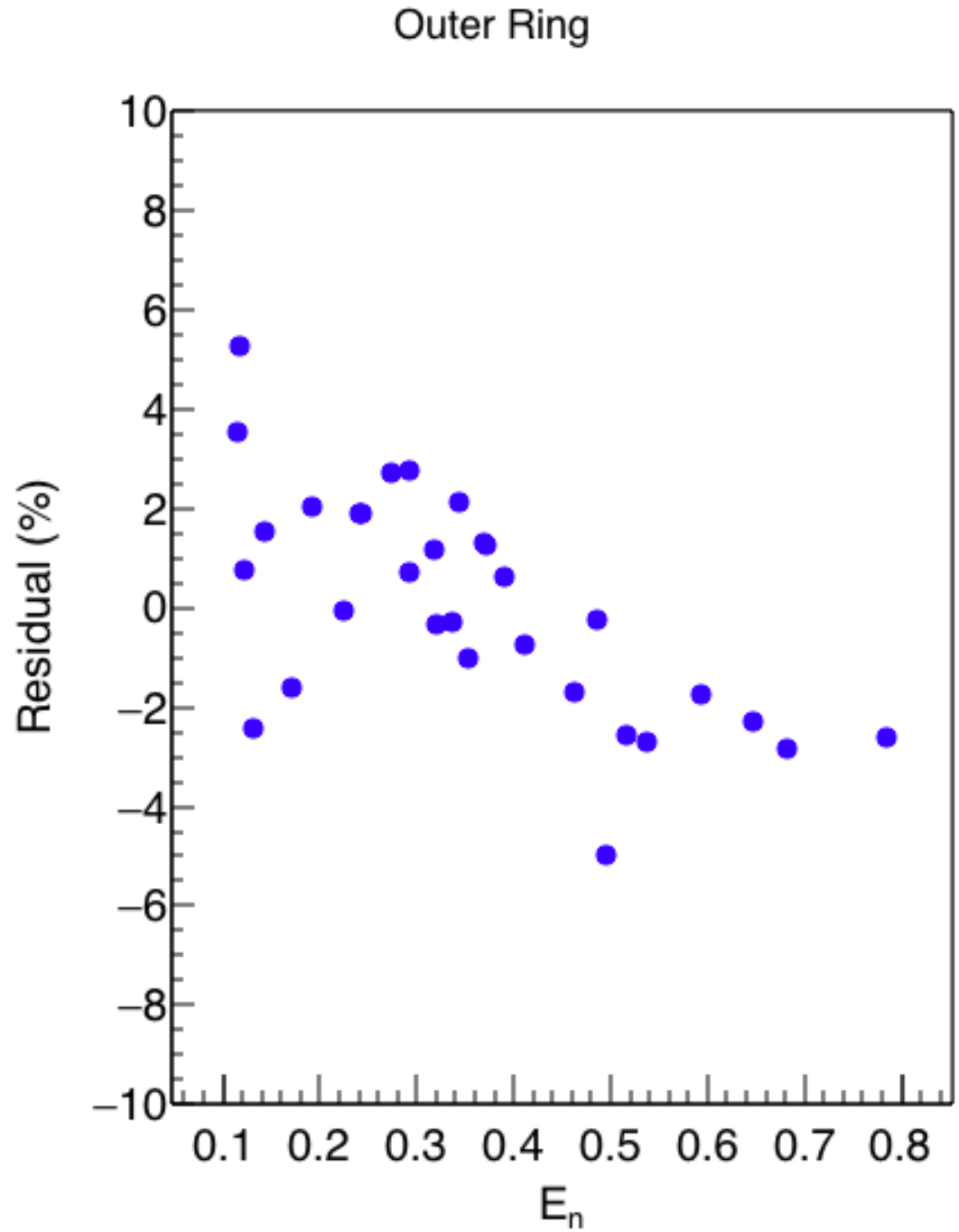
Outer Ring
Residual (%)
10
8
6
4
2
0
−2
−4
−6
−8
−10
0.1
0.2
0.3
0.4
0.5
0.6
0.7
0.8
E_n

Livermore Neutron Detector

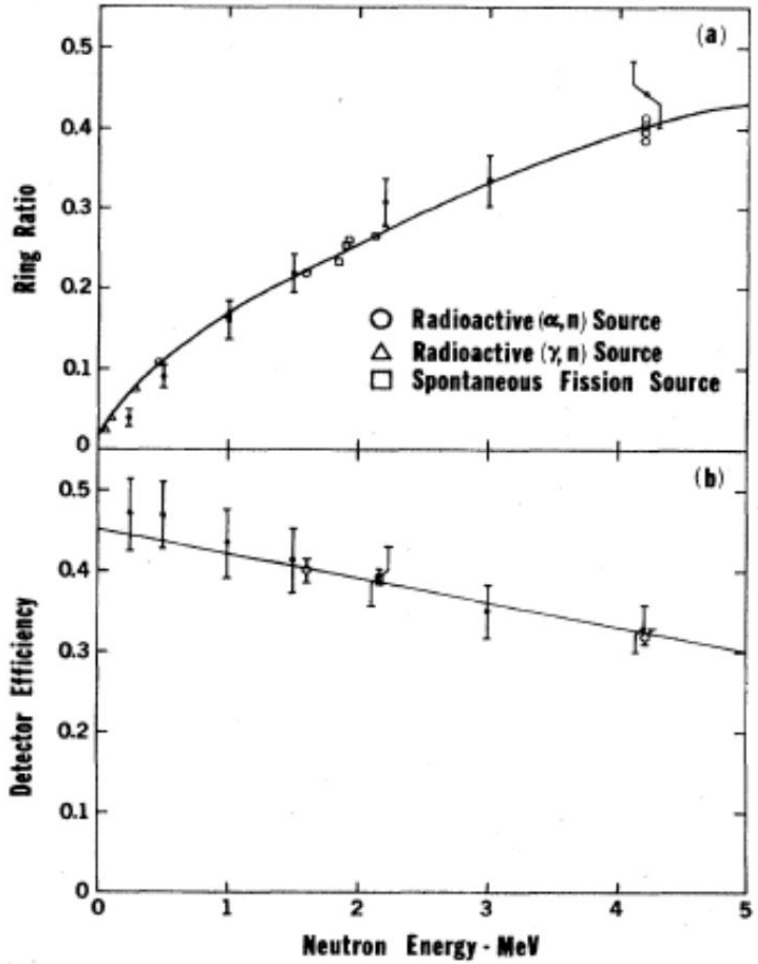

Berman & Fultz, Rev. Mod. Phys. 47, 713 (1975)

H. Utsunomiya *et al*'s Neutron Detector

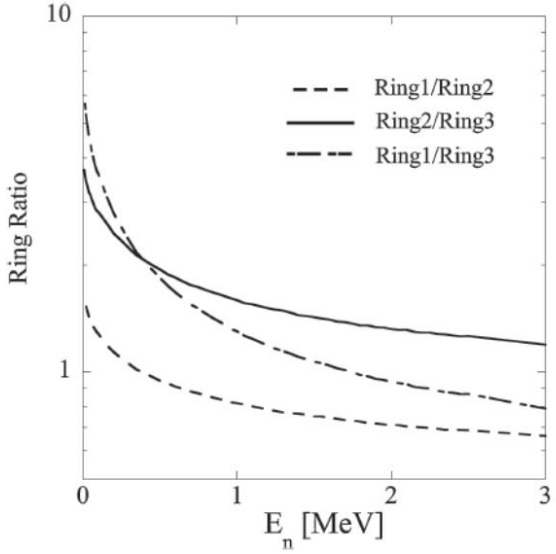

Fig. 5 MCNP Monte Carlo simulations of three ratios in neutron yield measured with Ring1, Ring2, and Ring3 of 4, 8, and 8 ^{3}He proportional counters, respectively, embedded in a polyethylene neutron moderator

O. Itoh et al., Journal of Nuclear Science and Technology 48, 834 (2011)

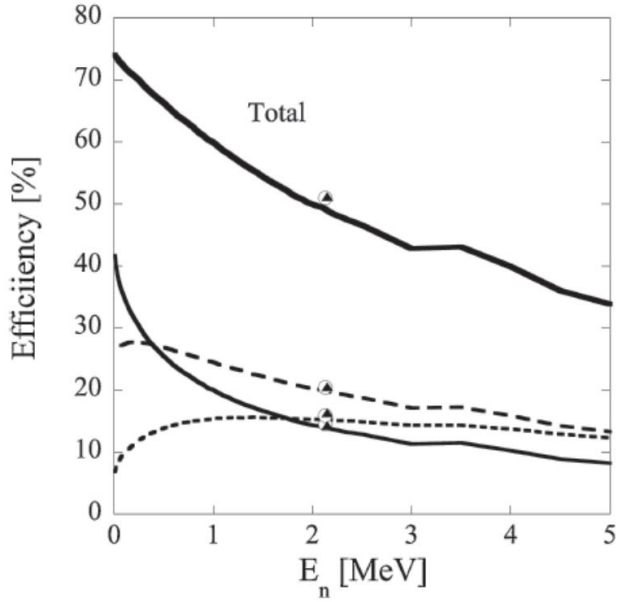

Fig. 4 Neutron detection efficiencies of Ring1 of 4 (solid curve), Ring2 of 8 (dashed curve), and Ring3 of 8 (dotted curve) ^{3}He proportional counters embedded in a polyethylene neutron moderator and the total efficiency. Results of the detection efficiency measurement with a ^{252}Cf neutron source are shown by open circles in comparison with MCNP Monte Carlo simulations (filled triangles).

$^{90}Zr(\gamma,n)^{89}Zr$

E_γ (MeV)	E_i (MeV)	$J_i^{\pi_i}$	E_{n_i} (MeV)	l_i	ϵ_{n_i} (%)	b_i	ϵ_n^{eff} (%)
12	0	$9/2^+$	0.03	3 (f wave)	52.89	1	**52.89**
12.1	0	$9/2^+$	0.13	3 (f wave)	52.15	1	**52.15**
12.2	0	$9/2^+$	0.23	3 (f wave)	51.53	1	**51.53**
12.4	0	$9/2^+$	0.43	3 (f wave)	49.21	1	**49.21**
12.5	0	$9/2^+$	0.53	3 (f wave)	47.69	1	**47.69**
12.8	0	$9/2^+$	0.82	3 (f wave)	44.18	0.17	**49.94**
	0.5878	$1/2^-$	0.24	0 (s wave)	51.12	0.83	
13	0	$9/2^+$	1.02	3 (f wave)	41.33	0.23	**46.94**
	0.5878	$1/2^-$	0.44	0 (s wave)	48.61	0.77	
13.5	0	$9/2^+$	1.51	3 (f wave)	36.71	0.26	**42.97**
	0.5878	$1/2^-$	0.93	0 (s wave)	42.68	0.45	
	1.0949	$3/2^-$	0.43	0 (s wave)	49.02	0.29	

$^{90}Zr(\gamma,n)^{89}Zr$

E_γ (MeV)	σ_{E_γ} (MeV)	$\sigma_{(\gamma,n)}$ (mb)	$\eta = \frac{\epsilon_{n_0}}{\epsilon_n^{\text{eff}}} = \frac{\sigma_{(\gamma,n)}}{\sigma_{(\gamma,n_0)}}$	
11.75	0.21	0.01 ± 0.01	1	
12	0.23	0.11 ± 0.01	1	
12.1	0.21	0.14 ± 0.02	1	
12.2	0.22	0.50 ± 0.03	1	
12.4	0.22	2.28 ± 0.12	1	
12.5	0.23	4.42 ± 0.24	1	
12.8	0.23	9.67 ± 0.52	0.88	**1** excited state
13	0.22	12.66 ± 0.68	0.88	**1** excited state
13.5	0.24	20.94 ± 1.13	0.85	**2** excited states

$^{90}Zr(\gamma,n)^{89}Zr$

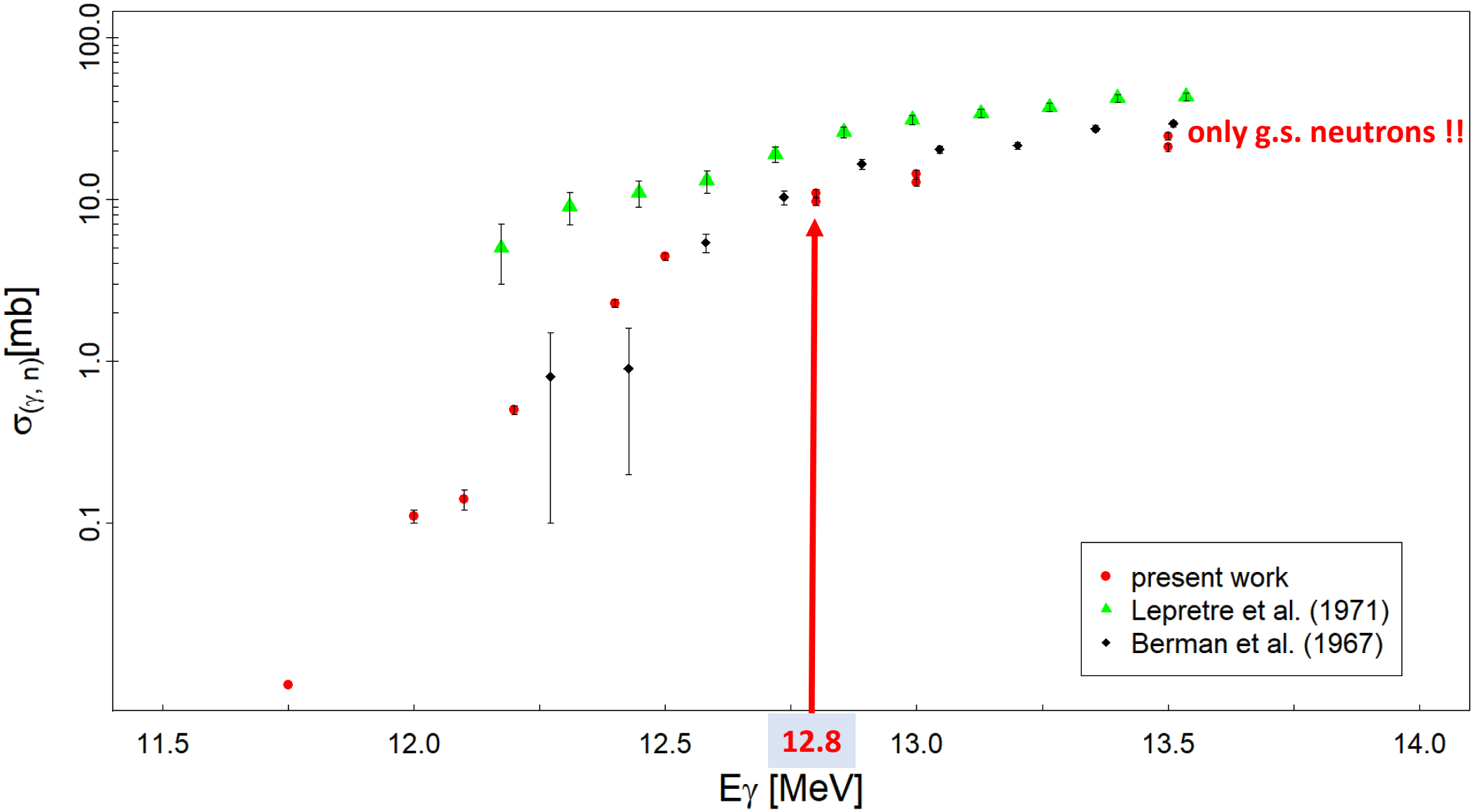

$^{94}Mo(\gamma,n)^{93}Mo$

E_γ (MeV)	σ_{E_γ} (MeV)	$\sigma_{(\gamma,n)}$ (mb)	$\eta = \frac{\epsilon_{n_0}}{\epsilon_n^{\text{eff}}} = \frac{\sigma_{(\gamma,n)}}{\sigma_{(\gamma,n_0)}}$	
9.5	0.18	0.28 ± 0.02	1	
9.6	0.17	1.21 ± 0.07	1	
9.65	0.17	2.51 ± 0.14	1	
9.7	0.17	2.97 ± 0.16	1	
9.75	0.17	4.50 ± 0.24	1	
9.8	0.17	4.93 ± 0.27	1	
9.85	0.17	6.28 ± 0.34	1	
9.95	0.16	7.83 ± 0.42	1	
10	0.19	8.44 ± 0.46	1	
10.2	0.17	10.11 ± 0.55	1	
10.5	0.17	11.77 ± 0.63	1	
10.8	0.17	13.06 ± 0.70	0.89	**1** excited state
11	0.17	14.53 ± 0.78	0.86	**1** excited state
11.5	0.24	17.47 ± 0.94	0.80	**3** excited states
11.65	0.25	18.73 ± 1.01	0.78	**3** excited states
11.8	0.22	20.63 ± 1.11	0.79	**3** excited states
11.95	0.23	22.61 ± 1.22	0.79	**6** excited states
12.25	0.22	24.20 ± 1.30	0.71	**8** excited states
12.5	0.23	27.86 ± 1.50	0.72	**11** excited states
12.8	0.23	32.39 ± 1.74	0.74	**14** excited states
13.5	0.24	48.64 ± 2.62	0.77	**22** excited states

$^{94}Mo(\gamma,n)^{93}Mo$

E_γ (MeV)	E_i (MeV)	$J_i^{\pi_i}$	E_{n_i} (MeV)	l_i	ϵ_{n_i} (%)	b_i	ϵ_n^{eff} (%)
9.7	0	$5/2^+$	0.02	1 (p wave)	53.79	1	**53.79**
9.75	0	$5/2^+$	0.07	1 (p wave)	53.29	1	**53.29**
9.8	0	$5/2^+$	0.12	1 (p wave)	53.03	1	**53.03**
9.85	0	$5/2^+$	0.17	1 (p wave)	52.44	1	**52.44**
9.95	0	$5/2^+$	0.27	1 (p wave)	51.45	1	**51.45**
10	0	$5/2^+$	0.32	1 (p wave)	50.30	1	**50.30**
10.2	0	$5/2^+$	0.52	1 (p wave)	47.74	1	**47.74**
10.5	0	$5/2^+$	0.81	1 (p wave)	44.03	1	**44.03**
10.8	0	$5/2^+$	1.11	1 (p wave)	40.51	0.59	**45.35**
	0.9433	$1/2^+$	0.18	1 (p wave)	52.32	0.41	
11	0	$5/2^+$	1.31	1 (p wave)	38.37	0.46	**44.73**
	0.9433	$1/2^+$	0.37	1 (p wave)	50.15	0.54	
11.5	0	$5/2^+$	1.80	1 (p wave)	34.35	0.31	**42.83**
	0.9433	$1/2^+$	0.87	1 (p wave)	43.23	0.37	
	1.4925	$3/2^+$	0.33	1 (p wave)	50.19	0.26	
	1.6950	$5/2^+$	0.13	1 (p wave)	52.18	0.06	
11.65	0	$5/2^+$	1.95	1 (p wave)	33.14	0.29	**42.46**
	0.9433	$1/2^+$	1.02	1 (p wave)	41.68	0.33	
	1.4925	$3/2^+$	0.47	1 (p wave)	48.39	0.28	
	1.6950	$5/2^+$	0.27	1 (p wave)	50.43	0.10	
11.8	0	$5/2^+$	2.10	1 (p wave)	32.25	0.29	**40.71**
	0.9433	$1/2^+$	1.17	1 (p wave)	39.94	0.30	
	1.4925	$3/2^+$	0.62	1 (p wave)	46.42	0.28	
	1.6950	$5/2^+$	0.42	1 (p wave)	49.04	0.13	
11.95	0	$5/2^+$	2.25	1 (p wave)	32.99	0.26	**41.57**
	0.9433	$1/2^+$	1.31	1 (p wave)	38.36	0.25	
	1.4925	$3/2^+$	0.77	1 (p wave)	44.66	0.24	
	1.6950	$5/2^+$	0.57	1 (p wave)	47.25	0.11	
	2.1420	$5/2^+$	0.129	1 (p wave)	52.30	0.04	
	2.1454	$3/2^+, 5/2^+$	0.125	1 (p wave)	52.32	0.07	
	2.1811	$3/2^+$	0.09	1 (p wave)	52.83	0.03	
12.25	0	$5/2^+$	2.25	1 (p wave)	29.54	0.23	**41.32**
	0.9433	$1/2^+$	1.61	1 (p wave)	35.57	0.16	
	1.4925	$3/2^+$	1.07	1 (p wave)	40.99	0.17	
	1.6950	$5/2^+$	0.87	1 (p wave)	43.44	0.08	
	2.1420	$5/2^+$	0.43	1 (p wave)	48.93	0.07	
	2.1454	$3/2^+, 5/2^+$	0.42	1 (p wave)	48.92	0.12	
	2.1811	$3/2^+$	0.39	1 (p wave)	49.72	0.12	
	2.4374	$1/2^+$	0.13	1 (p wave)	51.98	0.04	
	2.5297	$1/2^-, 3/2^-$	0.04	0 (s wave)	52.82	0.01	

A. Banu *et al.*, Phys. Rev. C 99, 025802 (2019)

$^{94}Mo(\gamma,n)^{93}Mo$

E_γ (MeV)	E_i (MeV)	$J_i^{\pi_i}$	E_{n_i} (MeV)	l_i	ϵ_{n_i} (%)	b_i	ϵ_n^{eff} (%)
12.5	0	$5/2^+$	2.79	1 (p wave)	28.78	0.23	**39.86**
	0.9433	$1/2^+$	1.86	1 (p wave)	33.87	0.10	
	1.4925	$3/2^+$	1.32	1 (p wave)	38.37	0.19	
	1.6950	$5/2^+$	1.12	1 (p wave)	40.45	0.06	
	2.1420	$5/2^+$	0.673	1 (p wave)	45.74	0.05	
	2.1454	$3/2^+, 5/2^+$	0.669	1 (p wave)	45.60	0.10	
	2.1811	$3/2^+$	0.63	1 (p wave)	46.26	0.10	
	2.4374	$1/2^+$	0.38	1 (p wave)	49.81	0.08	
	2.5297	$1/2^-, 3/2^-$	0.29	0 (s wave)	50.60	0.01	
	2.6190	$1/2^-, 3/2^-$	0.20	0 (s wave)	51.55	0.01	
	2.6701	$1/2^+$	0.15	1 (p wave)	52.15	0.04	
	2.7046	$1/2^+$	0.12	1 (p wave)	52.26	0.03	
12.8	0	$5/2^+$	3.09	1 (p wave)	27.66	0.28440	**37.16**
	0.9433	$1/2^+$	2.16	1 (p wave)	31.84	0.07408	
	1.4925	$3/2^+$	1.61	1 (p wave)	35.74	0.14420	
	1.6950	$5/2^+$	1.41	1 (p wave)	37.65	0.07771	
	2.1420	$5/2^+$	0.970	1 (p wave)	42.27	0.03704	
	2.1454	$3/2^+, 5/2^+$	0.966	1 (p wave)	42.25	0.07167	
	2.1811	$3/2^+$	0.93	1 (p wave)	46.46	0.06981	
	2.4374	$1/2^+$	0.68	1 (p wave)	45.92	0.06373	
	2.5297	$1/2^-, 3/2^-$	0.59	0 (s wave)	46.71	0.01074	
	2.6190	$1/2^-, 3/2^-$	0.50	0 (s wave)	48.01	0.00883	
	2.6701	$1/2^+$	0.45	1 (p wave)	48.90	0.05549	
	2.7046	$1/2^+$	0.41	1 (p wave)	49.35	0.05335	
	2.8421	$1/2^+$	0.28	1 (p wave)	50.66	0.04113	
	2.9552	$1/2^-, 3/2^-$	0.17	0 (s wave)	51.80	0.00499	
	3.0640	$1/2^-, 3/2^-$	0.06	0 (s wave)	52.66	0.00283	
13.5	0	$5/2^+$	3.78	1 (p wave)	25.35	0.32964	**32.93**
	0.9433	$1/2^+$	2.85	1 (p wave)	28.48	0.07525	
	1.4925	$3/2^+$	2.30	1 (p wave)	30.79	0.10762	
	1.6950	$5/2^+$	2.10	1 (p wave)	32.17	0.07133	
	2.1420	$5/2^+$	1.660	1 (p wave)	35.24	0.03091	
	2.1454	$3/2^+, 5/2^+$	1.659	1 (p wave)	35.27	0.05072	
	2.1811	$3/2^+$	1.62	1 (p wave)	35.53	0.04801	
	2.4374	$1/2^+$	1.37	1 (p wave)	38.07	0.04383	
	2.5297	$1/2^-, 3/2^-$	1.28	0 (s wave)	38.71	0.01244	
	2.6190	$1/2^-, 3/2^-$	1.19	0 (s wave)	39.69	0.00935	
	2.6701	$1/2^+$	1.14	1 (p wave)	40.15	0.04146	
	2.7046	$1/2^+$	1.11	1 (p wave)	40.43	0.04142	
	2.8421	$1/2^+$	0.97	1 (p wave)	42.03	0.04114	
	2.9552	$1/2^-, 3/2^-$	0.86	0 (s wave)	43.52	0.00869	
	3.0640	$1/2^-, 3/2^-$	0.75	0 (s wave)	44.92	0.00680	
	3.1592	$3/2^+, 5/2^+$	0.66	1 (p wave)	45.77	0.02017	
	3.3876	$3/2^+, 5/2^+$	0.43	1 (p wave)	48.92	0.01743	
	3.4503	$3/2^+, 5/2^+$	0.37	1 (p wave)	49.78	0.03078	
	3.5900	$1/2^-, 3/2^-$	0.23	0 (s wave)	50.66	0.00354	
	3.5963	$3/2^+, 5/2^+$	0.22	1 (p wave)	51.08	0.00348	
	3.7089	$3/2^+, 5/2^+$	0.11	1 (p wave)	52.06	0.00241	
	3.7200	$1/2^-, 3/2^-$	0.10	0 (s wave)	52.33	0.00229	
	3.7900	$1/2^-, 3/2^-$	0.03	0 (s wave)	52.57	0.00129	

A. Banu *et al.*, Phys. Rev. C 99, 025802 (2019)

$^{94}Mo(\gamma,n)^{93}Mo$

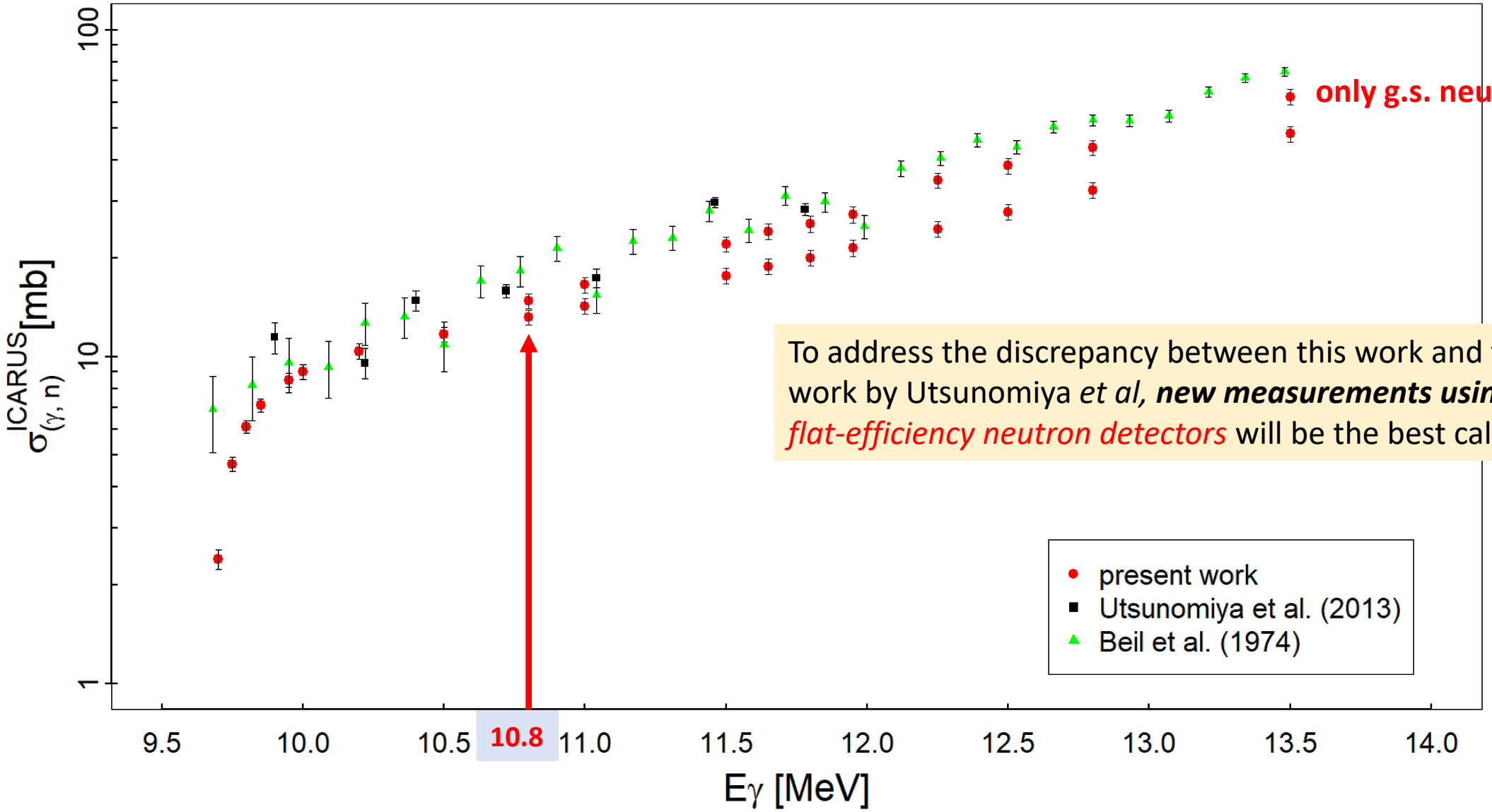

only g.s. neutrons !!

To address the discrepancy between this work and the work by Utsunomiya *et al*, ***new measurements using*** *flat-efficiency neutron detectors* will be the best call to action!

Nuclear Inst. and Methods in Physics Research, A 871 (2017) 135–141

Contents lists available at ScienceDirect

Nuclear Inst. and Methods in Physics Research, A

journal homepage: www.elsevier.com/locate/nima

Direct neutron-multiplicity sorting with a flat-efficiency detector

Hiroaki Utsunomiya [a,*], Ioana Gheorghe [b,c], Dan M. Filipescu [b], Tudor Glodariu [b], Sergey Belyshev [d], Konstantin Stopani [d], Vladimir Varlamov [d], Boris Ishkhanov [d], Seitarou Katayama [a], Daiki Takenaka [a], Takashi Ari-izumi [a], Sho Amano [e], Shuji Miyamoto [e]

[a] Department of Physics, Konan University, Okamoto 8-9-1, Higashinada, Kobe 658-8501, Japan
[b] ELI-NP, "Horia Hulubei" National Institute for Physics and Nuclear Engineering (IFIN-HH), 30 Reactorului, 077125 Bucharest-Magurele, Romania
[c] Faculty of Physics, University of Bucharest, RO-077125, Bucharest, Romania
[d] Lomonosov Moscow State University, Skobeltsyn Institute of Nuclear Physics, 119991 Moscow, Russia
[e] Laboratory of Advanced Science and Technology for Industry, University of Hyogo, 3-1-2 Kouto, Kamigori, Ako-gun, Hyogo, 678-1205, Japan

ARTICLE INFO

Keywords:
Neutron-multiplicity sorting
Flat-efficiency neutron detector
Partial photoneutron cross sections

ABSTRACT

A novel technique of direct neutron-multiplicity sorting with a flat-efficiency detector is proposed to resolve the long-standing discrepancy between the Livermore and Saclay data of partial photoneutron cross sections. A flat-response neutron detector with the detection efficiency of 36.5 ± 1.6% over a neutron energy range 0.01–5.0 MeV was developed by optimizing triple-ring configurations of He proportional counters embedded in a polyethylene moderator. The technique forms a foundation of measuring cross sections with $x = 1 - 3$ for the photonuclear data project of the International Atomic Energy Agency. The methodology of direct neutron-multiplicity sorting and key experimental elements are presented.

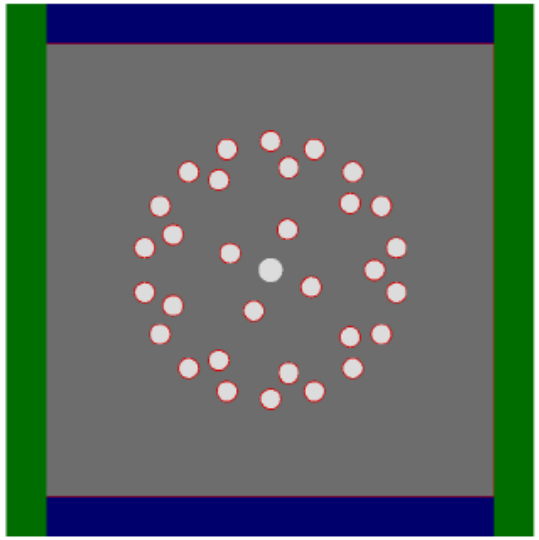

Fig. 1. (Color online) The layout of triple rings of ^{3}He counters for the flat-response neutron detector.

Fig. 2. (Color online) The experimental setup of the flat-response neutron detector.

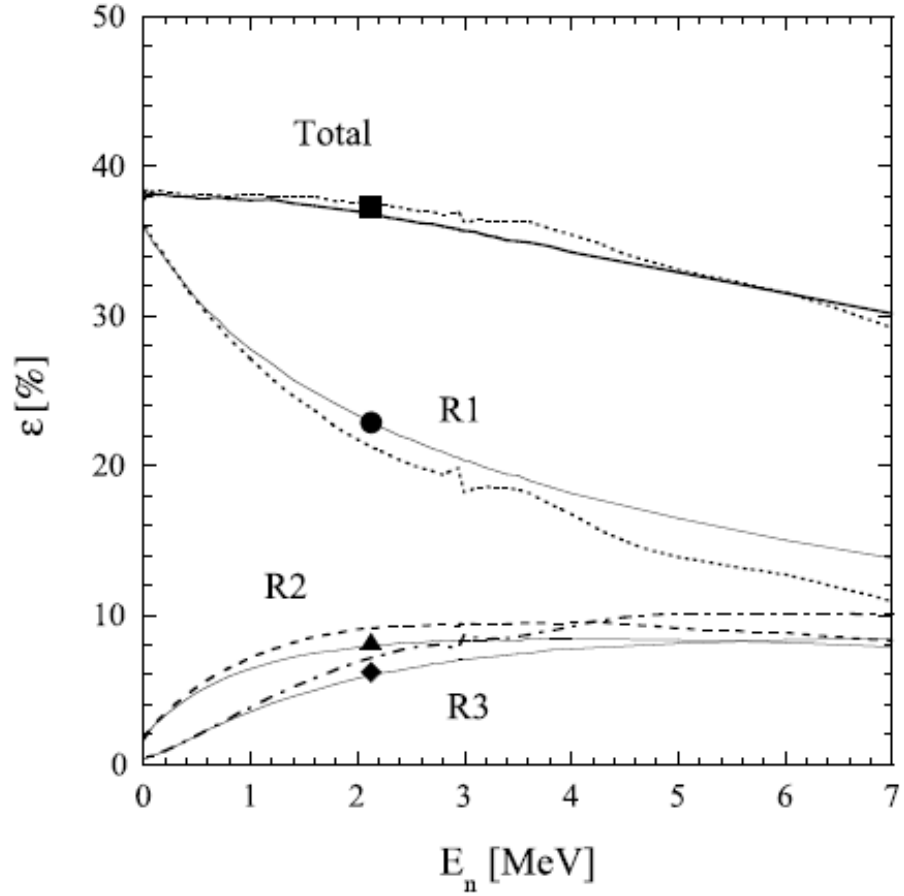

Fig. 3. The total detection efficiency and efficiencies of the individual rings of the flat-response neutron detector. Results of the calibration with a ^{252}Cf source are shown by the filled symbols. Results of the MCNP Monte Carlo simulations for monochromatic neutrons are shown by the broken lines, while those for the neutron-evaporation spectra by the solid lines.

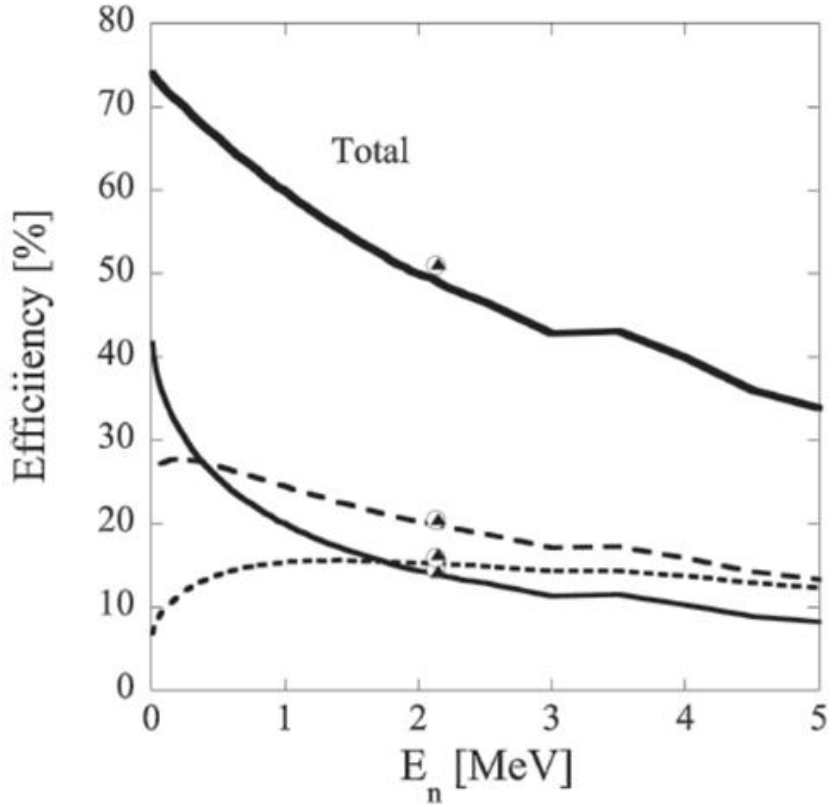

Fig. 4 Neutron detection efficiencies of Ring1 of 4 (solid curve), Ring2 of 8 (dashed curve), and Ring3 of 8 (dotted curve) ^{3}He proportional counters embedded in a polyethylene neutron moderator and the total efficiency. Results of the detection efficiency measurement with a ^{252}Cf neutron source are shown by open circles in comparison with MCNP Monte Carlo simulations (filled triangles).

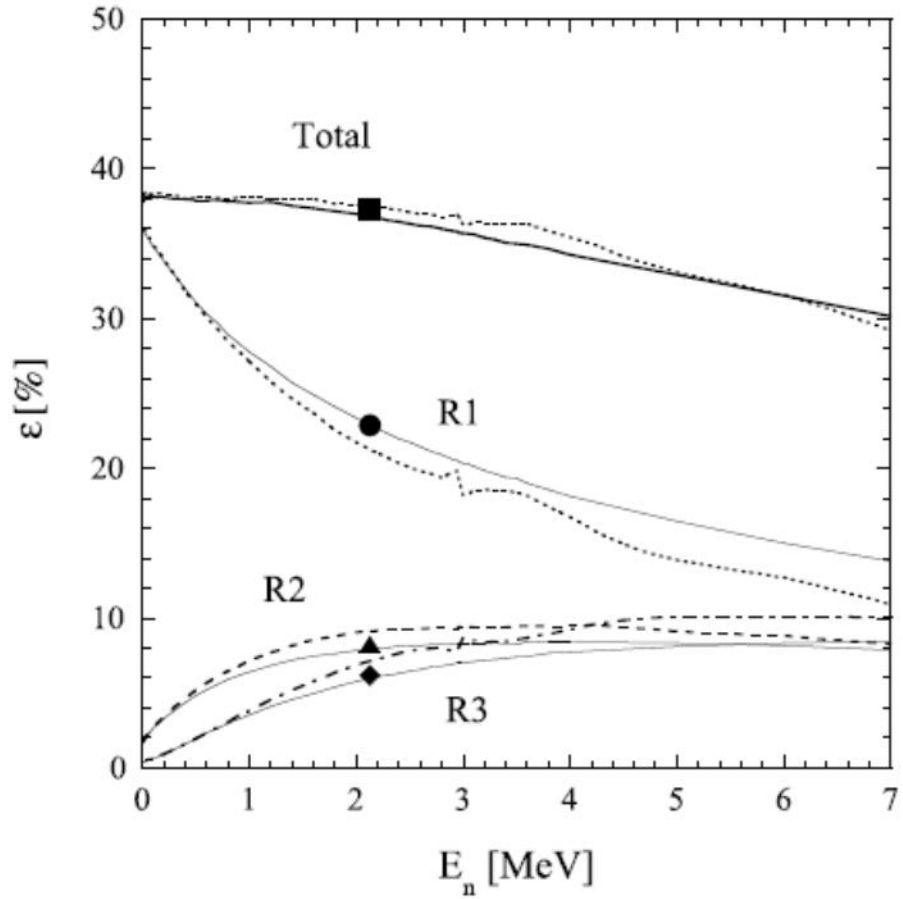

Fig. 3. The total detection efficiency and efficiencies of the individual rings of the flat-response neutron detector. Results of the calibration with a ^{252}Cf source are shown by the filled symbols. Results of the MCNP Monte Carlo simulations for monochromatic neutrons are shown by the broken lines, while those for the neutron-evaporation spectra by the solid lines.

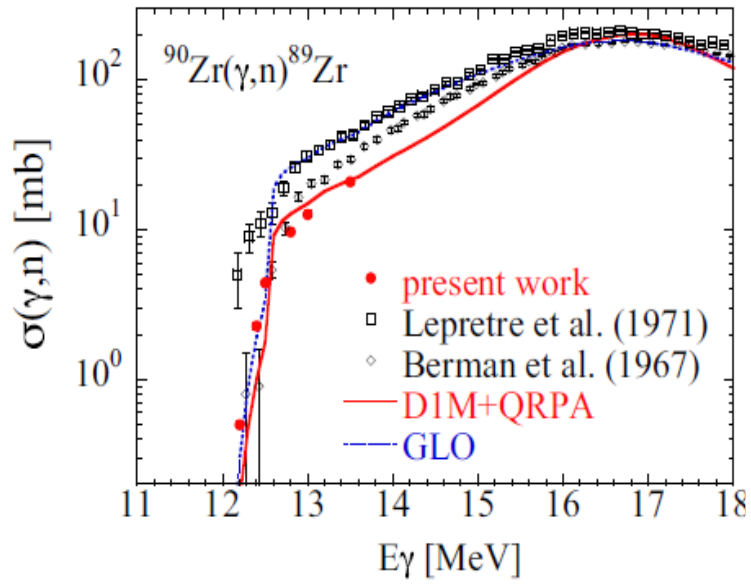

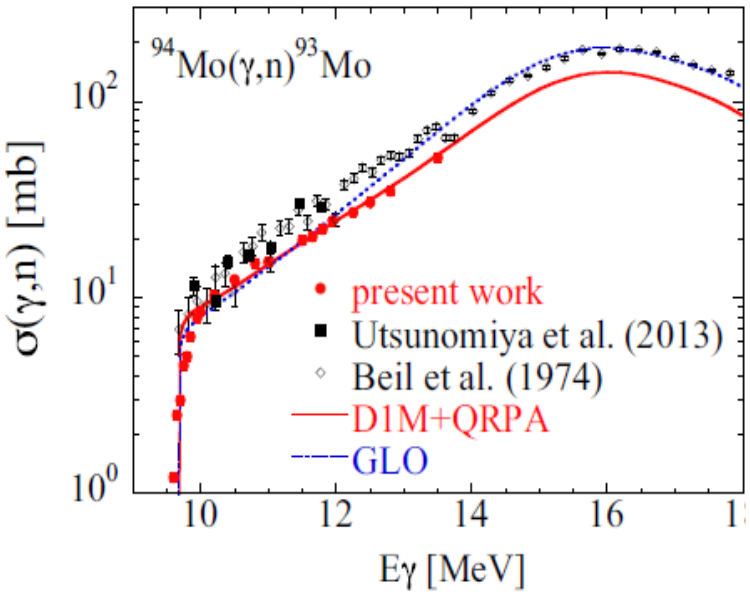

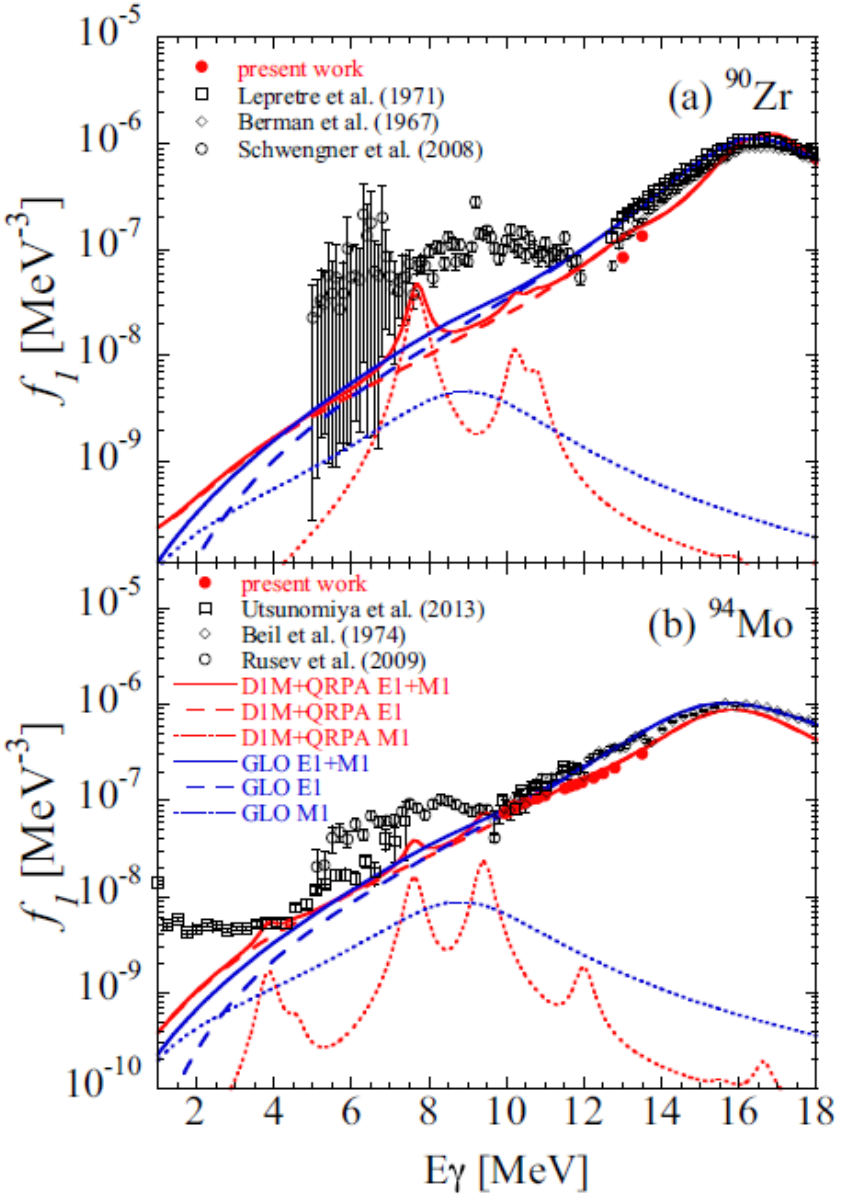

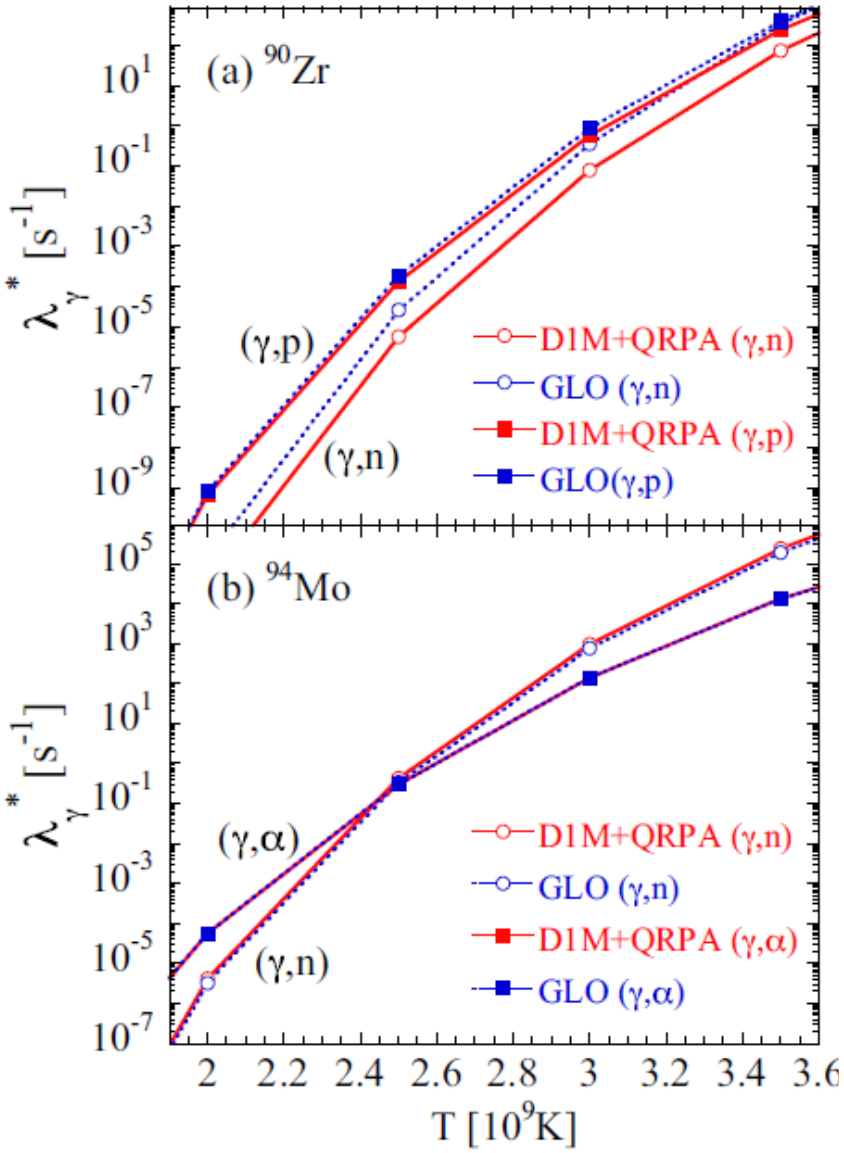

$$f(E_\gamma) = \frac{1}{3\pi^2\hbar^2c^2}\frac{\sigma_\gamma(E_\gamma)}{E_\gamma}$$

A. Banu *et al.*, Phys. Rev. C 99, 025802 (2019)

Acknowledgments

Research work for the ^{78,80}Kr(γ,γ') measurements is supported by the award no. DE-SC0021199

Research work for the ^{94}Mo(γ,n) and ^{90}Zr(γ,n) measurements was partially supported by the award no. 22662

Thank you for your attention!